Earth and Planetary Science Letters 528 (2019) 115788

Contents lists available at ScienceDirect

Earth and Planetary Science Letters

www.elsevier.com/locate/epsl

Importance of permeability and deep channel network on the distribution of melt, fractionation of REE in abyssal peridotites, and U-series disequilibria in basalts beneath mid-ocean ridges: A numerical study using a 2D double-porosity model

Boda Liu *, Yan Liang

Department of Earth, Environmental and Planetary Sciences, Brown University, Providence, RI 02912, United States of America

ARTICLE INFO

Article history:
Received 29 March 2019
Received in revised form 11 June 2019
Accepted 23 August 2019
Available online xxxx
Editor: B. Buffett

Keywords:
mid-ocean ridge
melting
porosity distribution
permeability anisotropy
rare earth elements
U series disequilibrium

ABSTRACT

A plethora of observations have been made at mid-ocean ridges and mantle sections of ophiolites: presence of tabular replacive dunites, highly depleted LREE in residual abyssal peridotites, U-series disequilibria in fresh basalts, crustal thickness, and highly attenuated seismic and magnetotelluric structures beneath spreading centers. These independent observations can become more powerful if they are jointly analyzed in a self-consistent model. The difficulty for such a model is to resolve and evaluate the effect of fine scale petrologic feature such as dunite channels in a tectonic scale geodynamic model. Here we present a two-dimensional double-porosity ridge model that consists of low-porosity residual lherzolite and harzburgite matrix and high-porosity interconnected channel network. The geodynamic simulation features a spatially distributed channel network and anisotropic permeability that gradually develops as the upwelling mantle is deformed. We compute the porosity, melt and solid flow fields for several choices of channel distribution and permeability model. We use the calculated porosity distribution and velocity fields to model the variations of REE in residual mantle and U-series disequilibria in melts.

The present study underscores the importance of deep channel networks and permeability model to the interpretation of first order geophysical and geochemical observations at mid-ocean ridge spreading centers. The anisotropic permeability of channels can enhance melt focusing by 60%, resulting in thicker crust. The attenuated seismic and magnetotelluric structures require a channel network starting from 60 km depth beneath the ridge axis. The depleted REE patterns in clinopyroxenes in residual abyssal peridotites are also consistent with melt extraction into channels starting from 60 km depth. Although deep channels are conducive to producing U-series disequilibria in eruptible melts, the present model still cannot explain the full ranges of the observed U series disequilibria data in MORB samples. Additional factors, processes, and models are discussed. And finally, we found that, within the uncertainty of the permeability, the porosity varies by three folds and the excess of ^{230}Th varies by up to two folds.

1. Introduction

The distribution of melt in the melting region is important to the interpretation of seismic and magnetotelluric structures beneath mid-ocean ridges (e.g. Forsyth et al., 1998; Key et al., 2013). The distribution and transport of melt depend on permeability of the partially molten region and style of melt migration (diffuse porous flow vs. channelized melt migration). Channelized melt migration is needed to preserve U-series disequilibria observed in fresh MORB samples and to account for the highly depleted LREE patterns in residual clinopyroxene (cpx) in abyssal peridotites (e.g. McKenzie, 1985; Johnson et al., 1990; Iwamori, 1993; Spiegelman and Elliott, 1993; Kelemen et al., 1997; Lundstrom, 2000). High porosity channels can be formed by reactive dissolution when melt produced in the deeper part of the melting region percolates through the mantle column (e.g. Aharonov et al., 1995; Kelemen et al., 1997). Tabular replacive dunites which are widely observed in the mantle sections of ophiolites may represent reactive dissolution channels (e.g. Kelemen et al., 1997, 2000). High-porosity channels can also be formed by shear-induced melt localization (e.g. Kohlstedt and Holtzman, 2009) and decompaction

---

* Corresponding author.
E-mail addresses: boda_liu@hotmail.com (B. Liu), yan_liang@brown.edu (Y. Liang).

https://doi.org/10.1016/j.epsl.2019.115788

at the lithosphere-asthenosphere boundary (LAB) (Sparks and Parmentier, 1991; Spiegelman, 1993; Hebert and Montési, 2010). These different melt localization mechanisms may operate in different parts of the melting region and may feed into each other to produce complex porosity and permeability structures beneath mid-ocean ridges (e.g. Kohlstedt and Holtzman, 2009).

A self-consistent model for melt generation, distribution, and extraction beneath mid-ocean ridges should be capable of explaining the following first-order geophysical and geochemical observations: crustal thickness, inferred melt distribution from seismic and magnetotelluric imaging, incompatible trace element abundances and U-series disequilibria in MORB, and highly depleted LREE in residual cpx in abyssal peridotites (e.g. Johnson et al., 1990; White et al., 1992; Lundstrom et al., 1995; Sims et al., 1995; Forsyth et al., 1998; Kelemen et al., 2000; Kohlstedt and Holtzman, 2009; Key et al., 2013; Elliott and Spiegelman, 2014; Elkins et al., 2019). Previous geodynamic or geochemical models for mid-ocean ridges use part of the aforementioned observations as constraints in individual studies. For example, most geochemical models for U-series disequilibria and REE depletion are 1D (e.g., McKenzie, 1985; Spiegelman and Elliott, 1993; Iwamori, 1993; Lundstrom, 2000; Jull et al., 2002). Where 2D geochemical models are used, the physical aspect of the model is highly simplified (e.g., constant porosity or diffuse porous flow, Richardson and McKenzie, 1994; Spiegelman, 1996; Behn and Grove, 2015). Most 2D geodynamic models for mid-ocean ridges focus on porosity distribution, solid and melt flow (e.g. Phipps Morgan, 1987; Spiegelman and McKenzie, 1987; Keller et al., 2017). It is not clear if these 2D geodynamic models can explain the first order geochemical observations at the mid-ocean ridges.

The key to connect geophysical and geochemical observations of mid-ocean ridges is the high-porosity channels. Keller et al. (2017) demonstrated the importance of reactive melt migration in a 2D ridge setting through numerical simulations. Although promising, direct numerical simulations of high-porosity channel formation over tectonic scale (100 km) face considerable challenges. The width of tabular replacive dunites observed in the field (10 cm to 200 m, Kelemen et al., 2000) is barely resolvable by typical numerical grid size. Consequently, the channels and their associated fine scale structures as documented in the field (Kelemen et al., 2000) and in outcrop-scale reactive dissolution simulations (e.g., Liang et al., 2010, 2011; Schiemenz et al., 2011) are under-resolved in the tectonic scale numerical simulations. The thermochemical models used in the reactive infiltration instability modeling are highly simplified that it is still not possible to make quantitative inference on the spatial distribution of high-porosity channels beneath mid-ocean ridges (e.g. Spiegelman et al., 2001; Liang et al., 2010, 2011). In this study we provide an interim solution to this difficult geodynamic-geochemical problem. We expand the 1D double-porosity model used in geochemical studies to 2D (e.g. Iwamori, 1993; Lundstrom, 2000; Jull et al., 2002; Liang and Parmentier, 2010). We will not explicitly model the formation of high-porosity channels. Instead, we prescribe a distribution of channels in the 2D domain, building on the current understanding of high-porosity channel formation in the mantle (Kohlstedt and Holtzman, 2009). Our main task is to examine the geodynamic and geochemical consequences of channelized melt migration beneath mid-ocean ridges. We use first-order geophysical and geochemical observations to constrain channel distribution in a trial of tests.

In a 2D distribution of channels, different regions of the channel network could have been formed by different mechanisms (Fig. 1a). The replacive channels formed by reactive infiltration instability is probably distributed in the upper part of the melting region. The depth has to be at least 30 km as MORB is undersaturated with orthopyroxene at low pressure (e.g. Kelemen et al., 1997). Deeper replacive channels (>60 km) can be formed if there is enough melt flux coming from below (e.g. Schiemenz et al., 2011; Keller et al., 2017). The shear-induced melt localization band probably exists in regions of high shear strain near the base of the lithosphere (Kohlstedt and Holtzman, 2009, shaded green regions in Fig. 1a). The permeability along the melt localization band should be greater than that along the direction perpendicular to the band. The third type of channel is decompaction channels formed along LAB (Sparks and Parmentier, 1991). The distribution of decompaction channels, the extent of permeability enhancement and anisotropy in regions of high shear strain, and the depth of replacive channels will be tested in this study.

The remaining part of this paper is organized as follows. In Section 2 and Appendix A, we introduce the 2D double-porosity ridge model that features spatially distributed high-porosity channels and permeability anisotropy. In Section 3, we examine the effect of channel distribution on crustal thickness, distributions of porosity, and melt and solid flow fields in the melting region. The effect of anisotropic permeability on melt focusing in association with variable mantle viscosity and spreading rate is also discussed. In Sections 4 and 5, we use observed REE patterns in residual abyssal peridotites and U-series disequilibria in MORB to further test the distribution of channels. We show that porosity distribution in the melting region, LREE depletion in residual cpx, and U-series disequilibria in eruptible melts are sensitive to the depth and permeability of channels. Based on the observed geophysical and geochemical constraints, we conclude that interconnected channel network starting from 60 km depth beneath the ridge axis is highly probable.

2. The double-porosity ridge model

The melting region beneath the mid-ocean ridge is treated as two overlapping continua (Iwamori, 1993; Lundstrom, 2000; Jull et al., 2002; Liang and Parmentier, 2010). The matrix continuum represents the melt-bearing residual lherzolite and harzburgite. The channel continuum represents the interconnected high-porosity channel network. The physical and chemical properties of the matrix and channel continua at a given point are defined in a local representative elementary volume that is larger than the channel width. Because the width of most dunite channels observed in the field is less than 100 m (e.g. Kelemen et al., 2000), the continuum representation of the channel network is valid as long as the size of the computation cell is much greater than 100 m (500 m in this study).

The model domain is illustrated in Fig. 1a. We assume a constant slope for LAB, which simplifies the solution for mantle flow (Spiegelman and McKenzie, 1987). The channel and matrix melts are collected into the decompaction channel at LAB. Base on Hebert and Montési (2010), we assume that the horizontally projected length of the decompaction channels (L_{dc}, referred as coverage length hereafter, Fig. 1a) is 100 km for a half-spreading rate of 50 mm/yr and 40 km for a half-spreading rate of 100 mm/yr. The shorter coverage length for fast spreading ridges is due to the large amount of crystallization of clinopyroxene and plagioclase over a short pressure interval under the thinner conduction lid of fast-spreading ridges (Hebert and Montési, 2010). Melts that encounter the base of the lithosphere outside of the coverage length of decompaction channels freeze at LAB. Following previous applications of double-porosity models for melt migration (Iwamori, 1993; Lundstrom, 2000; Jull et al., 2002; Liang and Parmentier, 2010), we will not solve for the distribution of channels, which requires knowledge of the poorly constrained matrix-channel transformation rate. Instead, we assume a distribution of channels in the model domain and use the model outcome to test the a priori assumption. This forward modeling allows us to explore the role of

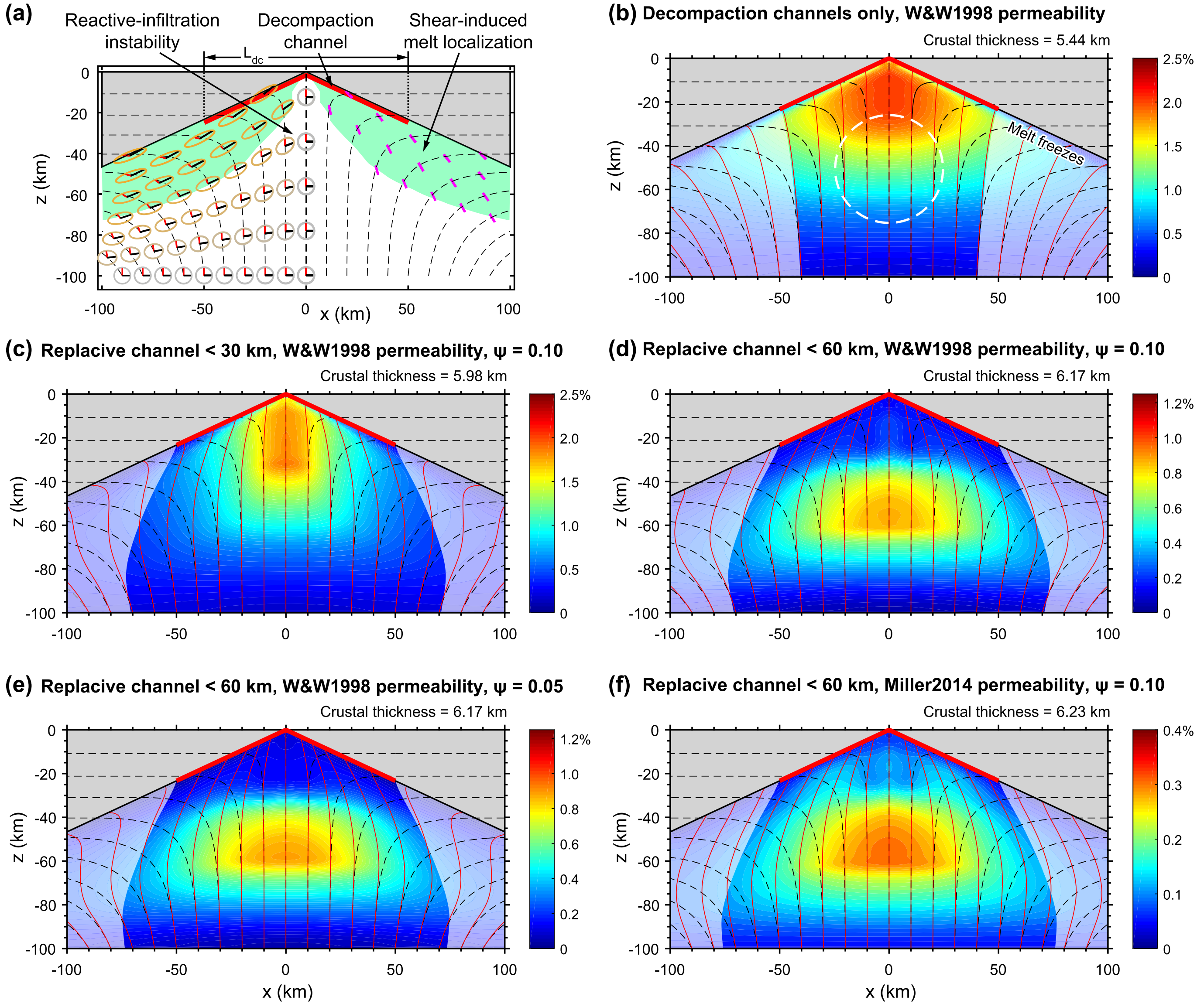

Fig. 1. Distribution of three types of channels beneath mid-ocean ridges (a) and calculated porosity distribution and streamlines of the solid and the melt using different combinations of channels and permeability models (Wark and Watson, 1998; Miller et al., 2014) (b-f). The bulk porosity shown in the color map combines the matrix and the channel continua. See Figs. S1 and S2 for melt flow field and porosity distribution in each continuum. Gray wedges are lithospheric mantle. Black dashed lines and thin red lines are streamlines of the solid mantle and the bulk melt combining the matrix melt and channel melt. The lateral bounds of the highlighted region beneath the decompaction channels are streamlines of matrix melt and channel melt wherever channel exists. Thick red lines represent the decompaction channels at LAB. The crust of ∼6 km thick is neglected in these figures. In panel (a), strain markers are placed at 100 km depth and deformed along the flow of the mantle. In the green shade regions, the shear strain corresponding to the simple shear component is greater than one. Magenta bars mark the orientation of shear-induced melt localization bands. The case in (b) has no replacive nor shear-induced channels. The white dashed circle outlines the approximate location of geophysically inferred high-porosity region (Yang et al., 2007; Key et al., 2013; Bell et al., 2016). Other cases have shear-induced channels in the region of high-shear strain and replacive channels starting from 30 km or 60 km depth. The volume proportion of channels ψ is either 5% or 10%. The porosity result of (d) and (f) are provided in the supplementary data file. (For interpretation of the colors in the figure(s), the reader is referred to the web version of this article.)

channel distribution on the first-order geophysical and geochemical observations of the mid-ocean ridge.

The governing equations, which are presented in Appendix A, include conservations of mass for the melt and solid in the matrix and channel continua, a momentum equation for the matrix and channel solid, and Darcy's law (Iwamori, 1993; Spiegelman and Elliott, 1993; Lundstrom, 2000; Liang and Parmentier, 2010). The matrix melting rate, which varies spatially in the 2D region, is calculated as the product of the upwelling rate and the melt productivity from pMELTS (Ghiorso et al., 2002). In the double-porosity model, part of the melt generated in the lherzolite and harzburgite matrix is sucked or extracted into nearby channels and this effect is quantified by the relative melt suction rate (Eq. (A.5)).

The distribution and transport of partial melt depend strongly on the permeability structure of the melting region. In the double-porosity ridge model, we assume that the permeability of the matrix continuum is isotropic whereas the permeability of the channel continuum is anisotropic. The isotropic part of permeability depends on grain size and porosity. In this study, we consider the permeability models of Wark and Watson (1998) and Miller et al. (2014) for the matrix continuum. For the range of porosity relevant to mantle melting (0.1∼1%), permeabilities based on the model of Miller et al. (2014) are 20-50 times those of Wark and Watson (1998).

The anisotropic part of permeability depends on channel orientation. In this study, we use a permeability tensor for the channel continuum, which has three degrees of freedom: the magnitudes at two principal axes and the orientation of the principal axes. In matrix notation, we have (Phillips, 1991):

$$\mathbf{k}_{\phi}^{ch} = \Theta^{T} \begin{bmatrix} k_{\phi}^{iso} + k_{\phi}^{add} & 0 \\ 0 & k_{\phi}^{iso} \end{bmatrix} \Theta, \tag{1}$$

$$\Theta = \begin{bmatrix} \cos(\theta) & \sin(\theta) \\ -\sin(\theta) & \cos(\theta) \end{bmatrix}, \tag{2}$$

$$k_{\phi}^{add} = \beta k_{\phi}^{iso}, \tag{3}$$

where k_{ϕ}^{iso} is the permeability of the channel in accordance to the porosity and grain size; k_{ϕ}^{add} is the magnitude of the additional permeability along the channel; Θ is the rotation tensor; θ is the dip of the easy-flow direction; and β, the permeability anisotropy, is an input parameter, accounting for the relative difference in permeability along the two principal axes. Eqs. (2) and (3) are standard expressions for rotational transformation of second order tensor (Nye, 1985).

The channel permeability anisotropy arises from the orientation of replacive channels and shear-induced channels. The orientation of replacive channels is mostly vertical as the melt is largely driven by buoyancy except near ridge axis at shallow depth. The orientation of shear-induced channels is determined by rotating the local shear plane 20° in the direction counter to the vorticity (e.g. Kohlstedt and Holtzman, 2009). The accumulated strain is an integral of the strain-rate along the streamline of the mantle. The anisotropic permeability ($\beta > 0$) only applies to regions where the shear strain is greater than one (green shaded regions in Fig. 1a). For convenience of numerical calculations, we use an error function to make a 5 km-wide smooth transition of β from zero to the assigned values at the boundary where the shear strain is one.

We use uniform grain size within each continuum as the kinetics of grain growth under deformation and in the presence of melt are not well constrained (e.g. Turner et al., 2015a). A range of grain size will be tested. In all cases, the channel has larger grain size, based on peridotite dissolution experiments (e.g. Morgan and Liang, 2005) and field observations of dunites in the mantle section of Oman ophiolite (e.g. Kelemen et al., 1997, 2000).

3. Melt distribution

The geophysically inferred porosity maximum is 50–70 km beneath the ridge axis (e.g. Forsyth et al., 1998; Yang et al., 2007; Key et al., 2013). The increase of porosity beneath the maximum has been attributed to upward increase in melt flux that results from small-degree hydrous melting below 60 km depth. However, the decrease of porosity above the maximum is still not well understood. Decompaction in response to the permeability barrier at LAB should occur within one compaction length which is on the order of 1 km (Sparks and Parmentier, 1991; Spiegelman, 1993). Therefore, the gradual porosity reduction over 50 km or more cannot be induced by the boundary condition at LAB. Here we show that the channel network inside the melting region controls the melt distribution.

To facilitate discussion, we first consider a reference case in which channels are absent in the melting region. The result is shown in Fig. 1b. The buoyancy dominates the pressure gradient generated by the flow of the mantle when the mantle viscosity is 10^{19} Pa·s (Phipps Morgan, 1987). Consequently, the flow of the melt relative to the solid is nearly vertical (thin solid red lines in Fig. 1b). An effective focusing mechanism could be the up-slope melt migration in the decompaction channels (Sparks and Parmentier, 1991; Spiegelman, 1993). Below the decompaction channels, the melt slightly diverges away from the vertical as it ascents through the porous matrix continuum in the melting region. The matrix porosity increases upward until the melt encounters the decompaction boundary layer at LAB. Melts generated outside the melt pooling area freeze at the LAB and are carried away by the lithosphere plate. The region of high porosity (>1.5%) is within 35 km of the ridge axis and centered at 20 km depth (Fig. 1b). The depth of the high-porosity center is above that of the observed geophysical anomalies (Fig. 1b).

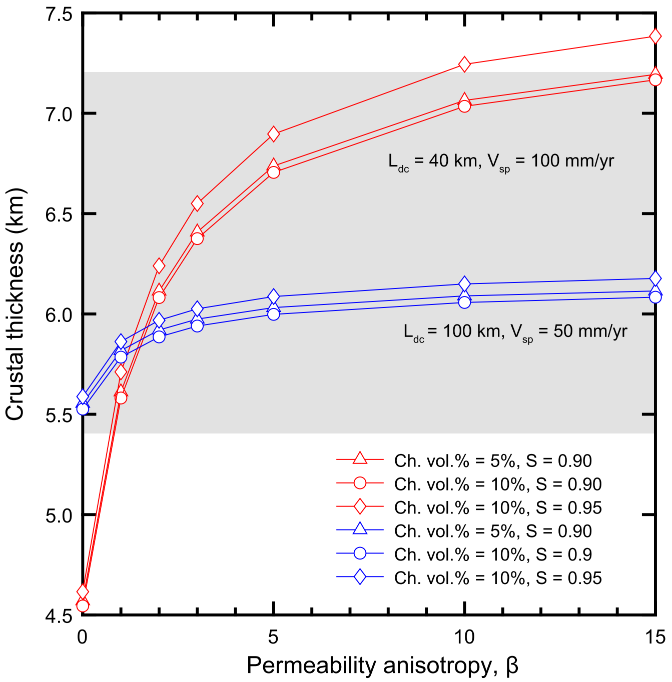

Fig. 2. Effect of channel permeability anisotropy on the crustal thickness. The gray shade is the range of observed crustal thickness (excluding Iceland) with half-spreading rate faster than 10 mm/yr (White et al., 1992). The wider coverage length of decompaction channels ($L_{dc} = 100$ km) are associated with the slower half-spreading rate ($V_{sp} = 50$ mm/yr). In these simulations, we assumed uniform channel proportion of 5% or 10% in the melting region. The relative melt suction rate ranges from 0.9 to 0.95. The mantle viscosity is 10^{19} Pa·s for all simulations.

The presence of high-porosity channels in the melting region reduces the porosity in the matrix and the bulk mantle (Figs. 1c-1f and supplementary Figs. S1 and S2). The bulk porosity is defined as:

$$\phi_{bulk} = (1 - \psi)\phi_m + \psi\phi_{ch}, \tag{4}$$

where ϕ is the porosity; ψ is the volume proportion of channel continuum; subscript m and ch represent the matrix and the channel, respectively. The bulk porosity is mainly controlled by the matrix porosity (cf. Fig. 1 vs. Figs. S1 and S2). The porosity in the channel contributes little to the bulk porosity (cf. Figs. S1a and S1b) due to the small volume fraction of the channel continuum (5-10%). The area of high porosity (>1.5%) is 70 km wide in the reference case of no channel continuum (Figs. 1b), whereas the area of high porosity is 30 km wide in the case with shear-induced channels and shallow (<30 km) replacive channels (Fig. 1c). Due to the smaller porosity and permeability in the matrix in regions with shear-induced channels, the flow of the matrix melt follows more closely to the streamlines of the mantle (cf. Figs. S1 and S2).

The melt extracted from the matrix to the channel can be effectively focused to the ridge axis because the shear-induced channels are orientated toward the ridge axis (Fig. 1a). As β, the permeability anisotropy, increases, the melt pooling region expands (Fig. S3). Consequently, more melt is focused to the axis. For 40-km wide coverage length of decompaction channels, the expanded

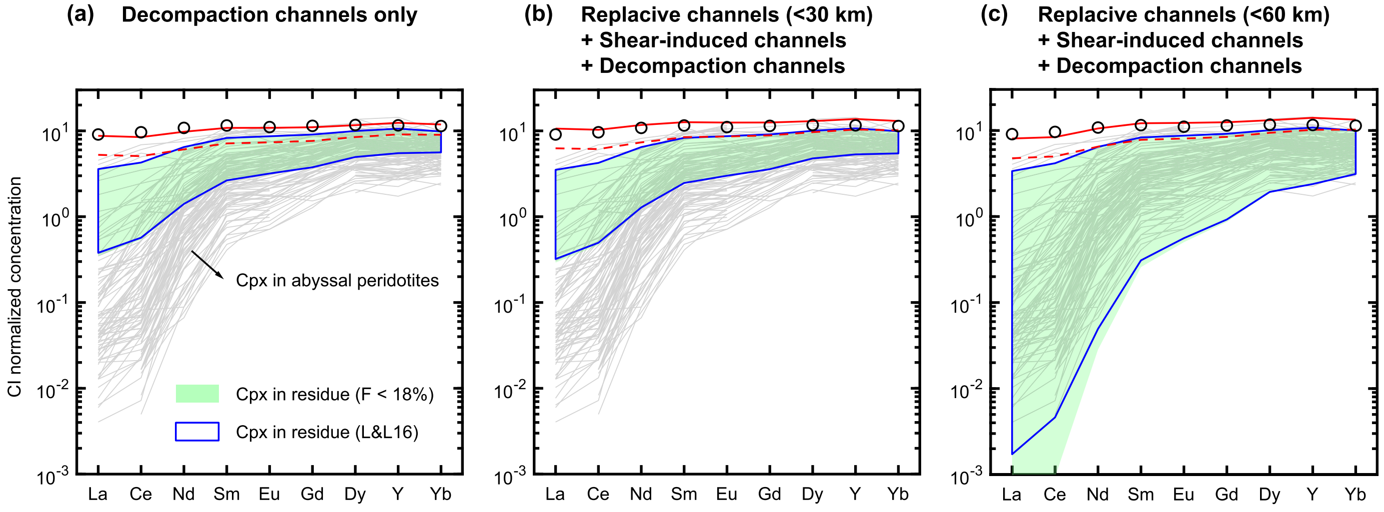
(a) Decompaction channels only

(b) Replacive channels (<30 km) + Shear-induced channels + Decompaction channels

(c) Replacive channels (<60 km) + Shear-induced channels + Decompaction channels

Fig. 3. Comparison of REE abundances in calculated pooled melt and residual clinopyroxene (cpx) with those from geochemical observations (Johnson et al., 1990; Johnson and Dick, 1992; Snow, 1993; Dick and Natland, 1996; Ross and Elthon, 1997; Seyler and Bonatti, 1997; Hellebrand et al., 2002, 2005; Salters and Dick, 2002; Brunelli et al., 2003, 2006; Warren, 2007; Brunelli and Seyler, 2010; Warren and Shimizu, 2010; Seyler et al., 2011; Lassiter et al., 2014; Mallick et al., 2014; D'Errico et al., 2016). The three panels correspond to cases shown in Figs. 1b, 1c, and 1d. REE abundances in residual cpx in abyssal peridotites are from the global compilation of Warren (2016). The green shade is the range of REE abundances in residual cpx calculated in the three cases. The blue outline marks the range of REE abundances calculated using an effective partition coefficient considering disequilibrium melting with a disequilibrium parameter for La of 0.01 (Liang and Liu, 2016). Circles are REE abundances in the bulk oceanic crust (White and Klein, 2014). The solid and dashed red lines are the calculated REE patterns in the pooled melt with the coverage length of decompaction channels of 100 km and 40 km, respectively. We use the starting mineral modes of Workman and Hart for DMM (2005), individual mineral/melt partition coefficient, and a linearized melting reaction (Baker and Stolper, 1994) to calculate the bulk partition coefficient of spinel lherzolite/harzburgite. For melting in the garnet stability field, we use pMELTS and DMM composition to derive garnet mode.

melt pooling region due to increasing β could include significant proportion of melt production region, resulting in 60% more melt focusing and up to 2.7 km thicker crust (Fig. 2). The wider (100 km) coverage length of decompaction channels has already covered most melt production region (Fig. S3). Therefore, increasing β results in only 11% more melt focusing (Fig. 2). In Fig. 2, we further demonstrate that the crustal thickness is not sensitive to channel volume fraction and matrix-to-channel melt suction rate.

While the melt extraction in regions of high shear strain controls the width of the high-porosity center in the melting region, the depth of replacive channels controls the depth of the high-porosity center. In a case with replacive channels extended to 60 km depth (Figs. 1d, 1e, and 1f), the maximum porosity in the matrix is at 57 km. Above the channel initiation depth, melt in the matrix can be continuously extracted to the channel at a rate higher than the matrix melting rate. Therefore, the porosity in the matrix decreases above the depth of channel initiation. When the channel forms at a greater depth, the porosity maximum in the matrix is smaller due to additional melt extraction. It is important to note that the location of maximum melting rate is not the same as the location of maximum porosity, as the latter also depends on the rate of melt extraction. The porosity should increase even if the melting rate decreases. It is the depth of zero net porosity increase due to the combined effect of melt production and melt extraction that controls the depth of the porosity maximum.

For the same grain size and channel distribution, the magnitude of porosity depends on the choice of permeability model. In general, the higher the permeability, the faster the melt flow and the lower porosity there will be in the melting region. In Figs. 1d and 1f we compare porosities derived from two widely used permeability models. The permeability model of Miller et al. (2014) is known to produce higher permeability than the model of Wark and Watson (1998). Figs. 1d and 1f show that the matrix and channel porosities calculated using the model of Miller et al. (2014) are 60% smaller than those derived from the model of Wark and Watson (1998). Figs. 1d and 1e show that reducing the volume proportion of channel continuum from 10% to 5% has little effect on the absolute magnitude of porosity. Therefore, the permeability model is essential for determining the absolute value of melt fraction in the melting region.

4. Rare earth elements

The spatial distribution of channels affects compositions of the pooled melt and residual solid. In this section we examine the role of channel distribution on REE abundances in the pooled melt and residual clinopyroxene (cpx). LREE are highly incompatible and hence very sensitive to the style of melting and melt extraction (e.g., Johnson et al., 1990; Kelemen et al., 1997). Given the melt distributions in Section 3 and the starting mantle composition (DMM from Workman and Hart, 2005), we consider three cases in this section: (1) decompaction channels only (Fig. 1b), (2) decompaction channels, shear-induced channels, and replacive channels above 30 km depth (Fig. 1c), and (3) decompaction channels, shear-induced channels, and replacive channels above 60 km depth (Fig. 1d). We show that only the case with deep replacive channels can reproduce the REE patterns observed in residual cpx from abyssal peridotites (Fig. 3). According to pMELTS, garnet is stable at depth greater than 80 km and its effect on trace element partitioning is considered in the trace element modeling discussed below.

4.1. REE in residual clinopyroxene

The salient feature of REE patterns in residual cpx in abyssal peridotites is the more than two-orders of magnitude depletion of La and Ce relative to HREE (Johnson et al., 1990; Johnson and Dick, 1992; Snow, 1993; Dick and Natland, 1996; Ross and Elthon, 1997; Seyler and Bonatti, 1997; Hellebrand et al., 2002, 2005; Salters and Dick, 2002; Brunelli et al., 2003, 2006; Warren, 2007; Brunelli and Seyler, 2010; Warren and Shimizu, 2010; Seyler et al., 2011; Lassiter et al., 2014; Mallick et al., 2014; D'Errico et al., 2016; Warren, 2016). Although melt-rock interaction in the lithosphere can explain some refertilized abyssal peridotites (30% of all samples, Warren, 2016), the LREE depletion in residual abyssal peridotites that show no obvious signs of refertilization (70% of all samples, Warren, 2016) is likely caused by fractional melting (Johnson et al., 1990). Fractional melting can be realized when the melt is not able to re-equilibrate with the minerals in the overlying melting column. Channelized melt migration is one physical mechanism to isolate newly formed matrix melt from its residual solid (Iwamori, 1993; Lundstrom, 2000). Following the streamline of the solid, the upwelling mantle undergoes batch melting before the initiation of the channels in the lower part of the melting region and fractional melting in the upper part of the melting region (Liang and Peng, 2010). In the case of decompaction channels alone (Fig. 1b) or the case with additional shallow (30 km) replacive channels and shear-induced channels (Fig. 1c), the extent of fractional melting experienced by residual matrix beneath the ridge axis is small (≤2.5%). These two cases cannot efficiently deplete LREE in residual cpx (Figs. 3a and 3b). This is consistent with the conclusion of Kelemen et al. (1997) who pointed out that at least 7% fractional melting is needed to reproduce the depleted LREE patterns in residual cpx in abyssal peridotites. In the case of deep (60 km) replacive channels (Figs. 1d), batch melting accounts for the first 2% of melting. Continuous melt extraction from 60 km depth to near the ridge axis results in a prolonged interval of fractional melting. Consequently, the case with deep replacive channels produces the range of LREE depletion as observed in natural samples (Fig. 3). The predicted pattern that fits the lower end of Nd to Yb has too low abundances of La and Ce (green shade at the bottom of Fig. 3c). The fit can be improved by introducing a small extent chemical disequilibrium between cpx and matrix melt which elevates the apparent bulk partition coefficients of La and Ce (Liang and Liu, 2016).

4.2. REE in pooled melt

REE abundances in well-mixed pooled melt are not very sensitive to channel distribution but depend moderately on the coverage length of decompaction channel (Fig. 3). All three cases can reproduce the REE abundances in the bulk oceanic crust (Workman and Hart, 2005; White and Klein, 2014). The case with 100 km coverage length produces higher REE abundances than the case with 40 km coverage length because more low-degree melts from shorter melting columns away from the ridge are focused to the ridge axis in the former case. This is essentially the shape effect of O'Hara (1985). In the case with deep replacive channels, the average degree of melting as defined by Forsyth (1993) with 100 km and 40 km coverage lengths are 7.0% and 11.9%, respectively. However, the difference in REE pattern between the two cases is comparable to the uncertainty in the input mantle composition (Workman and Hart, 2005). The crustal thickness produced in these two cases (6.17 to 6.89 km) are also within the normal range of observed oceanic crust (White et al., 1992). Therefore, the precise coverage length of decompaction channels cannot be constrained by the average melt composition. The coverage length of decompaction channels could also affect major element compositions of the pooled melt (Behn and Grove, 2015). Future models with joint constraints of major element and trace element compositions may shed new light to this problem.

5. U-series disequilibria

In this section, we further examine our 2D double-porosity ridge model through simulations of U-series disequilibria. We focus on ^{238}U series because there are constraints from two activity ratios and a range of half-lives of related nuclides. A noted difference between the present model and the previous models (Elliott and Spiegelman, 2014 and references therein) is the spatially distributed melt channels which control the porosity and the rate of melt extraction in the 2D melting region (Fig. 1). For a "dynamic melting model" with a porosity threshold above which the melt is extracted instantaneously, the following approximations for the activities in the matrix melt hold if the melting rate is slow (McKenzie, 1985):

$$\left({}^{230}\mathrm{Th}/{}^{238}\mathrm{U}\right) = \frac{\phi_m + k_{\mathrm{U}}}{\phi_m + k_{\mathrm{Th}}}, \tag{5}$$

$$\left({}^{226}\mathrm{Ra}/{}^{230}\mathrm{Th}\right) = \frac{\phi_m + k_{\mathrm{Th}}}{\phi_m + k_{\mathrm{Ra}}}, \tag{6}$$

where k_{U}, k_{Th}, k_{Ra} are bulk partition coefficients for U, Th, and Ra, respectively (Table 1 and Fig. 4). Eqs. (5) and (6) suggest that excess of ^{230}Th or ^{226}Ra in the matrix melt arises when the quotient in the right hand side is larger than one. Although Eqs. (5) and (6) are derived for the dynamic melting model with constant porosity, they are useful in understanding the roles of porosity and partition coefficient on the generation of these activity ratios in the present study.

Table 1
Partition coefficients for U and Th used in the 2D ridge model.

	Clinopyroxene	Orthopyroxene	Garnet
U	0.0103^{a}, $P < 1.5$ GPa 0.023^{b}, $P > 1.9$ GPa 0.0041^{d}, $P = 3$ GPa	0.0017^{b}	0.038^{c}, 0.0045^{d}
Th	0.012^{a}, $P < 1.5$ GPa 0.019^{b}, $P > 1.9$ GPa 0.0032^{d}, $P = 3$ GPa	0.0008^{b}	0.017^{c}, 0.0008^{d}

[a] From Hauri et al. (1994).
[b] From Wood et al. (1999).
[c] From Salters et al. (2002).
[d] From Pertermann et al. (2004).

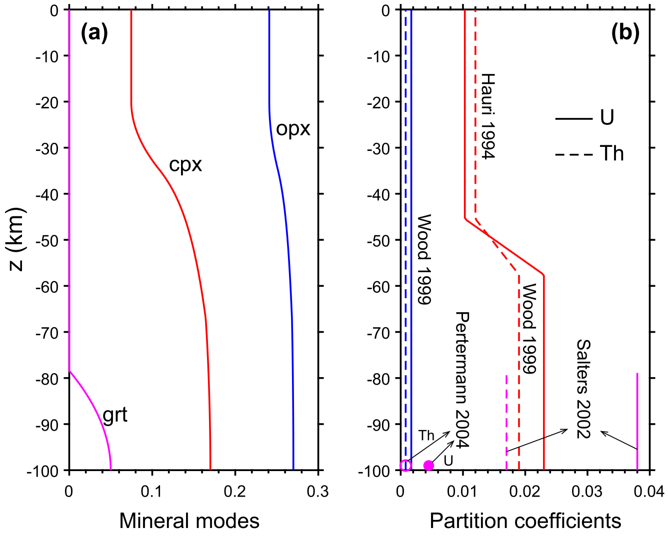

Fig. 4. Mineral modes (a) and partition coefficients (b) as a function of depth. For clarity, spinel and olivine are not shown. Mineral modes in the residue of DMM (Workman and Hart, 2005) are calculated using pMELTS (Ghiorso et al., 2002). Partition coefficients of U and Th are from Hauri et al. (1994), Wood et al. (1999), Salters et al. (2002), and Pertermann et al. (2004). Most simulations use partition coefficients in garnet (grt) from Salters et al. (2002) unless explicitly stated. The partition coefficient of Ra (not shown) is 1×10^{-4} (Wood and Blundy, 2014).

5.1. U-series disequilibria in the matrix melt

Large (^{230}Th/^{238}U) up to 1.40 exists near the bottom of the melting region (Figs. 5a, 5b, 5c, and Fig. S4a) where the porosity is small (Fig. 1) and Th is more incompatible than U due to

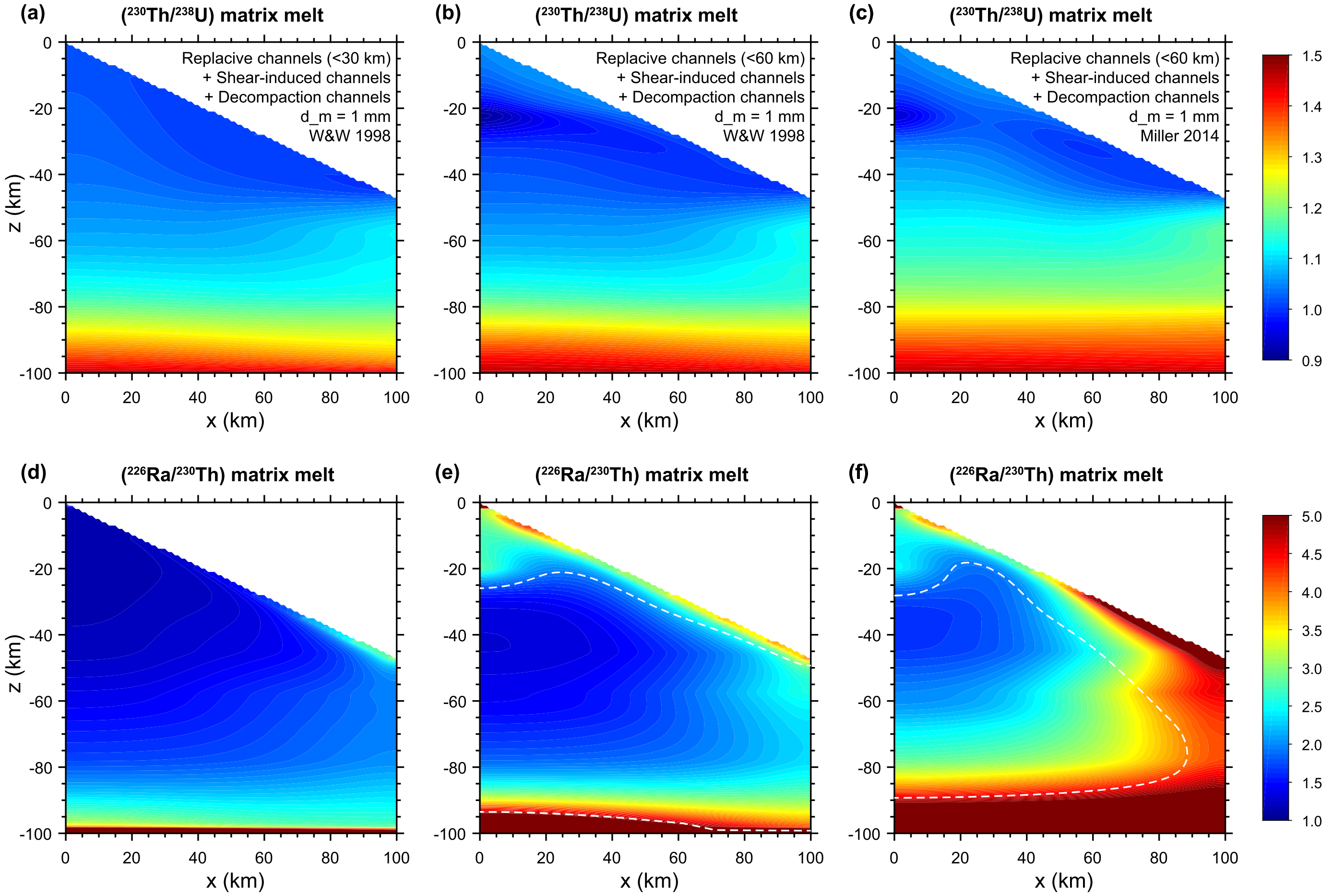

Fig. 5. Distribution of (^{230}Th/^{238}U) and (^{226}Ra/^{230}Th) in the matrix melt. The case in each column corresponds to the case shown in Figs. 1c, 1d, and 1f, respectively. Channel type, channels, matrix grain size, and permeability model (Wark and Watson, 1998; Miller et al., 2014) are labeled in the first row. White dashed lines in (e) and (f) mark the contour of 0.1% porosity, comparable to the partition coefficient of Th. For the case of the first column, smaller than 0.1% porosity only exists at LAB or at the bottom. The two cases with deep replacive channels produce thicker layer of high (^{230}Th/^{238}U) and (^{226}Ra/^{230}Th) at the bottom. The high-(^{226}Ra/^{230}Th) above 20 km depth and below LAB in the two cases with deep replacive channels is due to small matrix porosity.

the presence of garnet and high-pressure cpx (Fig. 4b). Garnet disappears above 80 km depth (Fig. 4a). The partitioning of Th and U in cpx could be reversed above 45 km depth (Fig. 4b, Hauri et al., 1994; Wood et al., 1999; Landwehr et al., 2001). Therefore, no (^{230}Th/^{238}U) greater than 1.2 exists above 45 km depth in our model predictions. The matrix melt with (^{230}Th/^{238}U) smaller than 1 in the case with deeper replacive channels (Figs. 4b and 4c) is due to the small matrix porosity and stronger incompatibility of U than Th at lower pressure. If Th is more incompatible than U throughout the depth interval from 100 km to the seafloor (Elliott and Spiegelman, 2014; Elkins et al., 2019), (^{230}Th/^{238}U) would be always greater than one. To provide a lower bound for (^{230}Th/^{238}U) in eruptible melts, we take a conservative approach by reversing the relative incompatibility of U and Th at pressure lower than 1.5 GPa (Fig. 4b). To the first order, the distribution of (^{230}Th/^{238}U) in the matrix melt calculated using the double-porosity ridge model is similar to that calculated using Eq. (4) (cf. Fig. 5 and Fig. S5). This similarity underscores the importance of matrix porosity in controlling (^{230}Th/^{238}U).

According to Eq. (6), the distribution of (^{226}Ra/^{230}Th) in the matrix melt reflects the distribution of matrix porosity normalized by the bulk partition coefficient of Th as Ra is highly incompatible ($k_{\mathrm{Th}} \sim 1 \times 10^{-3}, k_{\mathrm{Ra}} = 1 \times 10^{-4}$). There are three regions where the matrix porosity could be smaller than 0.1% (comparable to k_{Th}): the bottom, near LAB, and where there is strong melt extraction (Fig. 1). For the reference case with decompaction channels only (Fig. 1b) and the case with shallow replacive channels (Fig. 1c), noticeable region with matrix porosity smaller than 0.1% only exists near the bottom of the melting region. Therefore, (^{226}Ra/^{230}Th) greater than 2.5 only exists within 10 km at the bottom of the melting region for these two cases (Fig. 5d and Fig. S4d). If replacive channels starts from 60 km depth, more melt extraction occurs at depth and there are additional low porosity regions beneath the ridge axis: below LAB and laterally away from the center porosity maximum (Figs. 1d, 1e, and 1f). Consequently, deep replacive channels produce larger region with (^{226}Ra/^{230}Th) greater than 2.5 in the matrix melt (Fig. 5e and Fig. S5e). The approximation of McKenzie (1985) works almost perfectly for (^{226}Ra/^{230}Th) (cf. Fig. 5 and Fig. S5), further confirming the strong control of matrix porosity on (^{226}Ra/^{230}Th) in the matrix melt.

The matrix porosity used in the preceding discussion is based on the permeability model of Wark and Watson (1998). For the same grain size, the matrix porosity based on the permeability model of Miller et al. (2014) is 60% smaller (cf. Figs. 1d and 1f), resulting in an expansion of high-(^{230}Th/^{238}U) and (^{226}Ra/^{230}Th) in the 2D region. This is illustrated in Figs. 5c and 5f (also see Figs. S5c and S5f). For the same permeability model, the matrix porosity can be reduced by increasing grain size, which also results in an increase in (^{230}Th/^{238}U) and (^{226}Ra/^{230}Th) in the matrix melt (Fig. S6).

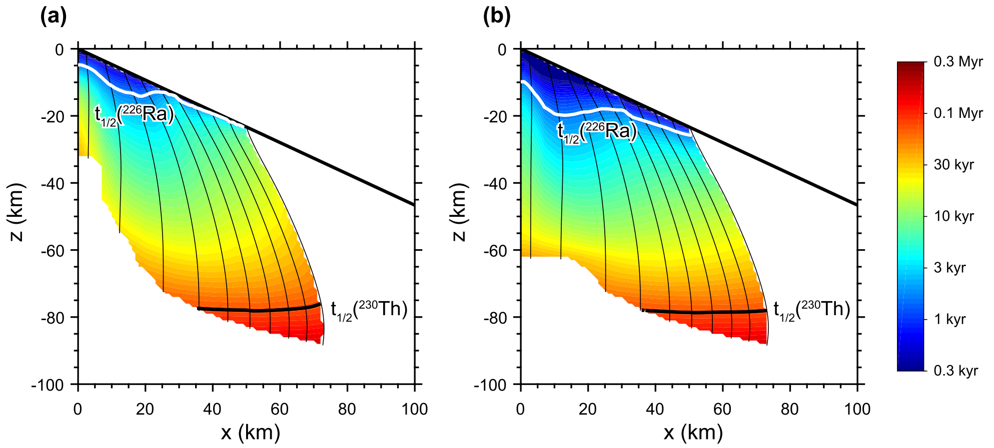

Fig. 6. The transport time in channels from the location of melt extraction to LAB. These two cases correspond to the case of Figs. 1c and 1d, respectively. Contours of the half-life of ^{230}Th and ^{22}Ra are shown as thick white and black lines. Thin lines are streamlines of the channel melt. The volume proportion of channels ψ is 10%. The channel grain size is 3 mm. The permeability model is from Wark and Watson (1998). The permeability anisotropy factor β is 5. Data for the transport time in the case of deep replacive channels (panel b) are provided in the supplementary data file.

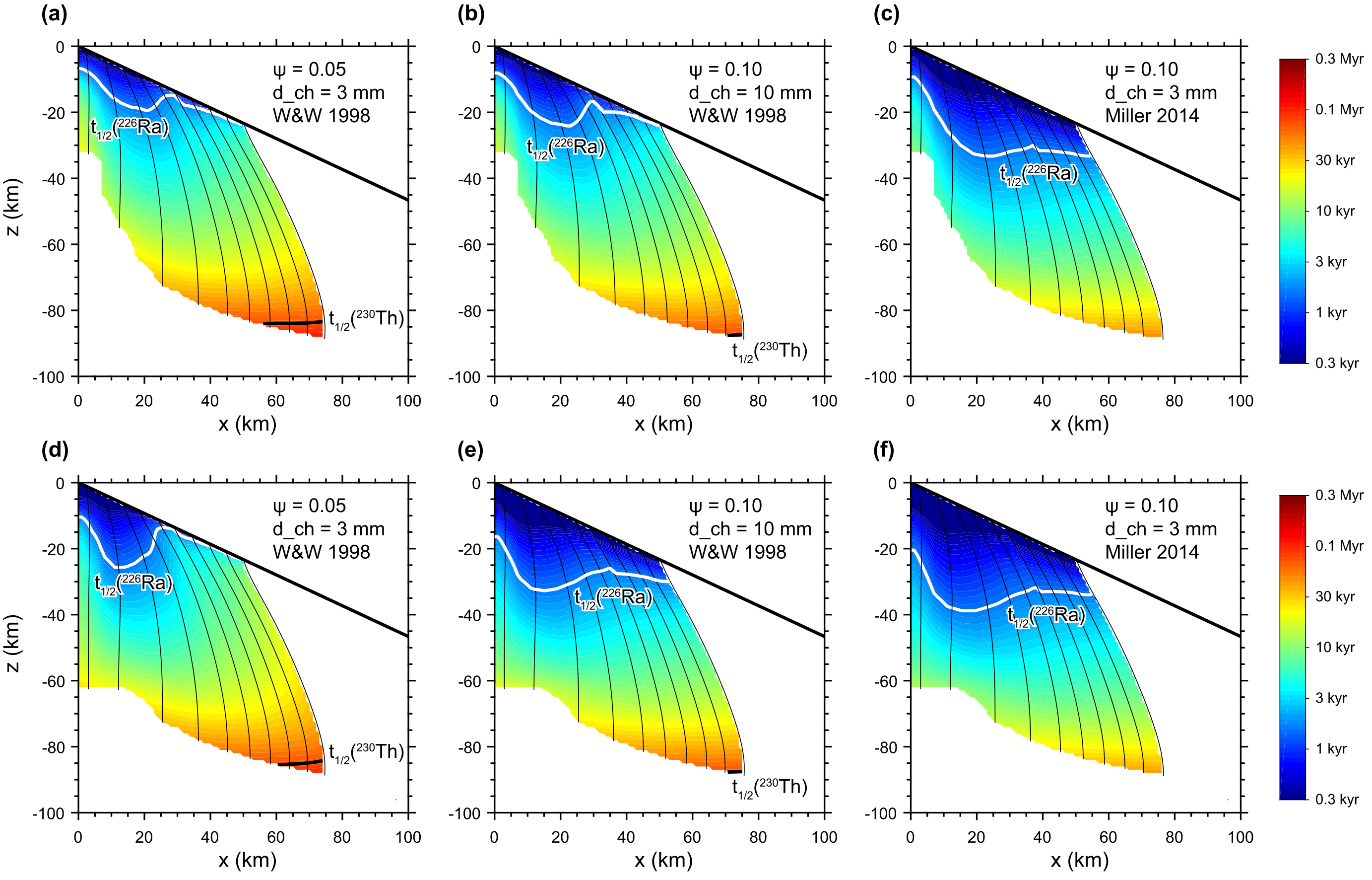

Fig. 7. Effects of channel volume proportion, channel grain size, and permeability model on the transport time in channels. The contours of the half-life of ^{230}Th and ^{22}Ra are shown as thick white and black lines. Thin lines are streamlines of the channel melt. The first and the second rows are comparable to Figs. 5a and 5b, respectively. The channel volume proportion ψ, channel grain size d_ch, and the permeability model of Wark and Watson (1998) or Miller et al. (2014) are labeled in each panel. Data for the transport time in the case of deep replacive channels with the permeability model of Miller et al. (2014) (panel f) are provided in the supplementary data file.

5.2. Transport time in channels

In the case with deep channel networks, compositions of matrix melts extracted at different locations define the largest possible range in which the aggregated channel melt could vary. (^{230}Th/^{238}U) and (^{226}Ra/^{230}Th) in the matrix melt will recover to unity at the time scale of the half-lives of ^{230}Th and ^{22}Ra, respectively, once the matrix melt is extracted to the channel. Therefore, it is important to keep track of every pocket of matrix melt from being extracted to the channel to being funneled into the decompaction channel and finally being transported to the ridge axis. The transport time of the extracted matrix melt in the channel continuum (called "transport time" hereafter) depends on the melt velocity as well as the location where the melt extraction occurs (Fig. 6). Matrix melts extracted in the region with transport time smaller than the half-lives of ^{226}Ra and ^{230}Th are likely to preserve

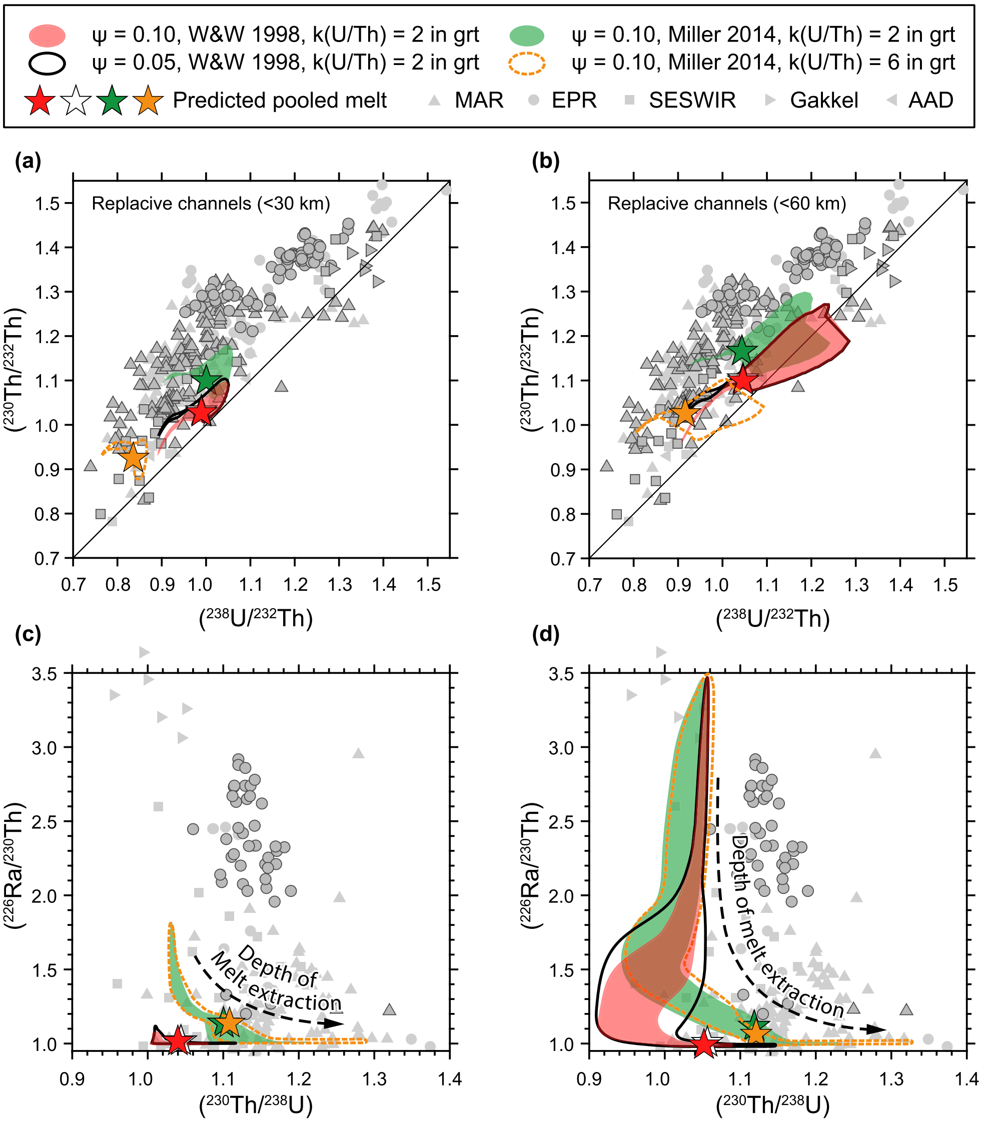

Fig. 8. Covariation of (^{238}U/^{232}Th) vs. (^{230}Th/^{232}Th) (first row) and (^{230}Th/^{238}U) vs. (^{226}Ra/^{230}Th) (second row) in eruptible melts after transport in channels. The grain size in the matrix and channel are 1 mm and 3 mm, respectively. The outline is the range of all eruptible melts. The pentagram is the composition of the pooled melt, averaged over all eruptible melts. The on-axis MORB data including Mid-Atlantic Ridge, East Pacific Rise, Southeast and Southwest Indian Ridges, Gakkel Ridge, and Australian-Antarctic Discordance are from the compilation by Elkins et al. (2019) and references therein cited in the text. Samples with age constraints are marked with black stroke. Four combinations of channel proportion, permeability model (Wark and Watson, 1998; Miller et al., 2014), and partition coefficients (Fig. 4) are listed in the legend. The fourth scenario uses the partition coefficients at high pressure from Pertermann et al. (2004).

most of their large (^{226}Ra/^{230}Th) and (^{230}Th/^{238}U), respectively. Therefore, it is informative to compare the map of transport time with the distribution of (^{226}Ra/^{230}Th) and (^{230}Th/^{238}U) in the matrix melt.

Matrix melts with (^{230}Th/^{238}U) > 1.25 are below 80 km depth (Fig. 5), which could hardly endure the transit through the channel network because the transport time is longer than the half-life of ^{230}Th if the grain size in the channel is 3 mm and the permeability model is from Wark and Watson (1998) (Fig. 6). The large (^{226}Ra/^{230}Th) of the matrix melt below 80 km depth will recover to unity as the transport time in channels is too long compared to the half-life of ^{226}Ra (Fig. 6). Only the high-(^{226}Ra/^{230}Th) matrix melt above 20 km depth in cases with deep replacive channels can escape the secular equilibrium during melt transport in the channel. The deep replacive channels beneath the ridge axis produces higher channel melt flux at shallow depth, which accelerates the channel melt and shortens the transport time from 20 km depth to the surface (cf. Figs. 6a and 6b). Therefore, deep replacive channels are important for preserving large (^{226}Ra/^{230}Th) in the pooled melt.

The transport time in the channels can be shortened if the volume proportion of channel continuum ψ is smaller (Fig. 6 vs. Figs. 7a and 7d). The porosity and the melt velocity in the channel increase as the flux of extracted melt is concentrated into smaller volume proportion of channels. However, due to the power law permeability, the change of channel melt velocity in response to 50% reduction in the channel volume fraction is small. Alternatively, melt velocity in the channel can be faster if the grain size in the channel is larger (Fig. 6 vs. Figs. 7d and 7e) or the permeability model changes from Wark and Watson (1998) to Miller et al. (2014) (Fig. 6 vs. Figs. 7c and 7f). The faster channel melt velocity extends the region with transport time smaller than the half-life of ^{230}Th to deeper than 80 km. Therefore, large excess of ^{230}Th can be better preserved with smaller channel volume fraction or larger permeability in channels or a combination of the two.

5.3. Covariations of activity ratios

This section examines covariations of activity ratios in eruptible melts and pooled melt. The eruptible melts are unmixed matrix melts extracted into the channel at different locations in the melting region. The eruptible melts have considered the decay of U series during melt transport in channels. The pooled melt is the average of all eruptible melts weighted by the melt flux. The eruptible melts and the pooled melt represent two endmember scenarios in which every possible melt composition either remains unmixed during transport or these melts are efficiently mixed during their transport in channels and residence in the crustal magma chamber. The pooled melt and most eruptible melts are plotted above the equiline in the diagram of (^{238}U/^{232}Th) vs. (^{230}Th/^{232}Th) (Figs. 8a and 8b, see also Fig. S7). The melt extracted deep has (^{230}Th/^{238}U) up to 1.50 and (^{226}Ra/^{230}Th) close to one while the melt extracted shallow has (^{230}Th/^{238}U) close to one and (^{226}Ra/^{230}Th) much greater than one (Figs. 8c and 8d). Because of the strong incompatibility of U, Th, and Ra, the melt extracted shallow has little abundance of these elements. The pooled melt as a mixture of all eruptible melts has (^{230}Th/^{238}U) slightly larger than one and (^{226}Ra/^{230}Th) much closer to one compared to the range of all eruptible melts (Fig. 8).

Matrix melt with large (^{230}Th/^{238}U) at 80 km depth can preserve (^{230}Th/^{238}U) up to 1.33 after melt transport (Fig. 8d). (^{230}Th/^{238}U) is slightly greater than one or even slightly smaller than one in matrix melts above 60 km depth. Because of the short half-life of ^{226}Ra, only the melt extracted shallow can have (^{226}Ra/^{230}Th) noticeably greater than one. Therefore, (^{226}Ra/^{230}Th) in all eruptible melts decreases with the depth of melt extraction. Due to more melt extraction in the case with deeper replacive channels, (^{226}Ra/^{230}Th) in the shallow matrix melt is higher, resulting in higher (^{226}Ra/^{230}Th) of up to 3.5 in the eruptible melts (Fig. 8d). The model of Jull et al. (2002) also found that large (^{226}Ra/^{230}Th) exists in shallow low-porosity matrix melt.

Increasing the partition coefficient of U relative to that of Th in garnet can result in smaller U/Th in the eruptible melts and pooled melt (Figs. 8a and 8b). Additional melt extraction in the case of deeper replacive channels could fractionate U/Th to higher values in the eruptible melts. The range of (^{230}Th/^{238}U) in the eruptible melts could increase by 10%. However, (^{230}Th/^{238}U) in the matrix melt above 80 km depth tends to be reset by the partitioning of U and Th in cpx. The (^{230}Th/^{238}U) in the eruptible melts extracted above 80 km is modestly affected by the change of the partition coefficients of U and Th in garnet.

The choice of the permeability model has a strong effect on (^{230}Th/^{238}U) and (^{226}Ra/^{230}Th) in eruptible melts (Fig. 8). The permeability model of Miller et al. (2014) produces smaller matrix porosity and consequently, larger (^{230}Th/^{238}U) and (^{226}Ra/^{230}Th) in the matrix melt than the permeability model of Wark and Watson (1998). Further, the permeability model of Miller et al. (2014) promotes faster channel melt velocity compared to the permeability model of Wark and Watson (1998).

5.4. Comparison with MORB data

Some inferences can be made by comparing the variations of activity ratios observed in MORB with those predicted by the 2D ridge model. The present result cannot reproduce some MORB with (^{238}U/^{232}Th) greater than 1.3. If a mantle source with higher U/Th ratio is used (e.g., U/Th = 2.9, Stracke and Salters (2004) vs. 2.5 from Workman and Hart (2005), the latter is used in the present study), the predicted (^{238}U/^{232}Th) will be 16% higher. The increase of U/Th would not change (^{230}Th/^{238}U) and (^{226}Ra/^{230}Th) because the initial condition for nuclides in ^{238}U series is secular equilibrium, which is independent of U/Th ratio in the homogeneous mantle source. Therefore, predicted melt compositions would shift to the northeast by up to 0.23 unit in response to the increase of U/Th in the source in Figs. 8a and 8b. A comparison between cases with different depths of replacive channels (cf. Figs. 8a and 8b) suggests that channels deeper than 60 km beneath the ridge axis could be important for the MORB data below the equiline (Fig. 8b).

The values of (^{230}Th/^{238}U) and (^{226}Ra/^{230}Th) in MORB extend to 1.38 and 3.7, respectively (Rubin and Macdougall, 1988; Goldstein et al., 1989, 1992, 1993; Bourdon et al., 1996, 2000, 2005; Lundstrom et al., 1998, 1999; Sturm et al., 2000; Peate et al., 2001; Cooper et al., 2003; Rubin et al., 2005; Russo et al., 2009; Dreyer et al., 2013; Waters et al., 2013; Turner et al., 2015b; Elkins et al., 2011, 2014, 2016a, 2016b; Scott et al., 2018). Larger (^{230}Th/^{238}U) than present results can be produced by further increasing the ratio of the partition coefficient of U relative to that of Th in the minerals (e.g. cpx at low pressure and garnet) or by increasing the proportion of clinopyroxene and garnet in the mantle source through lithological heterogeneity (Elkins et al., 2019). Increase of channel permeability and depth may also produce larger (^{230}Th/^{238}U). Larger channel permeability could result from larger grain size (Fig. S7) or greater permeability anisotropy than what have been used in current simulations.

Although current model produces (^{226}Ra/^{230}Th) up to 3.5 in the eruptible melts, the abundances of Ra and Th in these melts would be too low compared to MORB. The predicted pooled melt has (^{226}Ra/^{230}Th) no greater than 1.1 which is much smaller than many of the MORB samples (Fig. 8c and 8d). Large (^{226}Ra/^{230}Th) in the pooled melts would require less than 1.6 kyr melt transport time from deeper part of the melting region where the matrix porosity has to be small and the concentration of Ra and Th in the low-degree matrix melt are relatively high. These two conditions are not met in results presented so far (Figs. 1 and 7).

One possible mechanism to produce large (^{226}Ra/^{230}Th) in the melt while maintaining high (^{230}Th/^{238}U) is through shallow level melt-cumulate interaction (Saal and Van Orman, 2004). This process can increase (^{226}Ra/^{230}Th) in the pooled melt by 2 (Saal and Van Orman, 2004) while having little modification of (^{230}Th/^{238}U). Interestingly, samples from Gakkel Ridge (Elkins et al., 2014) where there could be a thick lithosphere have some of the highest (^{226}Ra/^{230}Th) observed.

Another mechanism that may increase (^{226}Ra/^{230}Th) in the melt is by increasing the effective partition coefficient of Th through disequilibrium melting (Qin, 1992; van Orman et al., 1998; Liang and Liu, 2016). This condition can be realized when diffusion of the divalent Ra in cpx is faster than that of Th. The diffusivity of Th in cpx is similar to those of U and La in cpx (van Orman et al., 1998, 2001). Inversion of REE patterns in cpx in residual abyssal peridotites has revealed the presence of a small extent of chemical disequilibrium for La in cpx during near fractional melting (Liang and Liu, 2016; Liu and Liang, 2017). Hence the effect of chemical disequilibrium helps in producing large (^{226}Ra/^{230}Th). Most EPR samples with age constraints have 1.10-1.18 (^{230}Th/^{238}U) and 1.5-3.0 (^{226}Ra/^{230}Th) (Goldstein et al., 1989, 1992, 1993; Sims et al., 1995; Sims et al., 2002; Dreyer et al., 2013; Scott et al., 2018). The pooled melt produced in the current model with the permeability model of Miller et al. (2014) has similar (^{230}Th/^{238}U) of 1.10-1.12 but (^{226}Ra/^{230}Th) close to one (Figs. 8c and 8d). Therefore, a combination of melt-cumulate interaction in the crust and disequilibrium melting in the mantle can produce the trend of increasing (^{226}Ra/^{230}Th) at relatively constant (^{230}Th/^{238}U) as observed in EPR.

Melts generated 80 km away from the axis at 60 km depth could have (^{226}Ra/^{230}Th) of 3.5 and (^{230}Th/^{238}U) of 1.2 in the case with deep replacive channels (Figs. 5c and 5f). These melts are outside the region that can be sampled by the decompaction channels (side regions not highlighted in Figs. 1b-1f). However, if the coverage length increases or there are additional melt extraction mechanisms that can sample the outside regions beyond the coverage of decompaction channels, the eruptible melts could have higher (^{226}Ra/^{230}Th) and (^{230}Th/^{238}U). In an endmember scenario in which melt transport is effectively instantaneous and melts in the entire model domain are focused to the axis, the eruptible melts would be represented by all matrix melts in the melting region (Fig. 5) and the highest (^{226}Ra/^{230}Th) and (^{230}Th/^{238}U) observed in MORB would be reproduced (Fig. S8). The crustal thickness is insensitive to the increased coverage length because regions of high melting rate are within the 100 km coverage length (Fig. S3). Therefore, increasing the coverage length or letting part of the melt generated outside of the coverage length at LAB to be transported to the ridge axis is capable of reproducing the range of U series disequilibria observed in MORB.

6. Summary and further discussion

We have simulated melting and melt migration beneath mid-ocean ridges using the double-porosity ridge model that features spatially distributed high-porosity channels and permeability anisotropy. Three types of channels are considered: decompaction channels at LAB, replacive channels in the melting region, and shear-induced channels. We have demonstrated that the inferred melt distribution from seismic and magnetotelluric imaging beneath mid-ocean ridges, the highly depleted LREE in residual cpx in abyssal peridotites, and the range of (^{230}Th/^{238}U) in MORB can be explained if there exists a deep channel network in the melting region. The crustal thickness and the average REE in the crust are not particularly sensitive to channel distribution. The range of (^{226}Ra/^{230}Th) in the eruptible melts generated by the present model is consistent with the range of (^{226}Ra/^{230}Th) in MORB. However, the pooled melt that mixes all eruptible melts has too small (^{226}Ra/^{230}Th) compared to MORB data. Other processes such as cumulate-melt interaction in the crust, disequilibrium melting, or sampling small-degree melts from regions beyond the coverage of decompaction channels in the mantle may be needed to account for the observed large (^{226}Ra/^{230}Th) in MORB.

The depth of replacive channels is controlled by the reactivity or solubility of mantle pyroxene with respective to melts generated in the underlying mantle, the amount of pyroxene present in the matrix continuum, and the magnitude of matrix melt flux (Schiemenz et al., 2011). Higher reactivity, lesser mantle pyroxene, and larger melt flux favor deeper replacive channels. Such a condition may be realized when the upwelling mantle is heterogeneous consisting of fertile (more fusible) and refractory (less pyroxene) domains of variable size and distribution. The existence of enriched blobs is generally consistent with the interpretation of radiogenic isotopic ratios in MORB and abyssal peridotites (Liu and Liang, 2017; Sanfilippo et al., 2019). The stronger partitioning of U over Th in enriched lithologies could also increase ^{230}Th excess (Elkins et al., 2019). Therefore, mantle heterogeneity is important for understanding both geochemical observations and melt migration processes.

The present study underscores the importance of permeability model to the first order geophysical and geochemical observations of mid-ocean ridges. The matrix porosity and the channel melt velocity are sensitive to the permeability in the matrix and the channel continua. Changing the permeability model from Wark and Watson (1998) to Miller et al. (2014) results in 60% less porosity in the matrix and an increase of (^{230}Th/^{238}U) in the eruptible melts from 1.09 to 1.23. Nonetheless, both permeability models are calibrated for mono-mineralic aggregates. Presence of pyroxene is likely to reduce the matrix permeability (Zhu and Hirth, 2003), increasing the porosity in the melting region. Therefore, more work on permeability model, especially for olivine + pyroxene + melt aggregate with anisotropic fabric, is needed to reconcile geophysical observations and U-series disequilibria. Because the permeability depends on grain size squared, the grain sizes of the matrix and channel are also important.

As a first 2D double-porosity model for mid-ocean ridges, we have made a number of assumptions and simplifications in this study: (1) the solid viscosity is constant and uniform; (2) the flow fields of the matrix and channel are symmetric about the ridge axis and independent of time; (3) the coverage length of decompression channel, the permeability anisotropy factor β, and the melt suction rate are prescribed; and (4) the channel formation processes are not modeled. In reality, the mantle flow could be asymmetric about the ridge axis (e.g. Forsyth et al., 1998) and the mantle viscosity could vary in response to changes in melt fraction, strain, and composition. As the mantle flow affects the formation of shear-induced channels, the permeability tensor has yet to be quantified and tested against laboratory deformation experiments. In regions with high shear strain at shallow depth where both shear and reaction induced melt localization may operate concurrently, the distribution of channels may be more complicated than that considered in the current model (Kohlstedt and Holtzman, 2009). Finally, there are other mechanisms for channelized melt migration that are not considered in the present study but may help to explain U-series equilibria in MORB. These include hydrofractures, vug waves, solitary waves, and compaction-dissolution waves (e.g. Kelemen et al., 1997; Hesse et al. 2011; Phipps Morgan and Holtzman, 2005). More studies are needed to test if deep replacive channels can form or other transport mechanisms are responsible for the delivery of the melt from below 60 km depth beneath the ridge axis.

Acknowledgements

We thank Don Forsyth, Marc Parmentier, Alberto Saal, Mark Behn, and Greg Hirth for useful discussion. Thoughtful review by Lynne Elkins helped to improve this manuscript. This work was supported by National Science Foundation grants EAR-1624516 and OCE-1852088.

Appendix A

We consider concurrent melting and melt migration in a double-porosity mantle in which the volume fraction of interconnected high-porosity channels is ψ. For simplicity, we assume that the solid in the channel is moving with the solid in the matrix (i.e., $\mathbf{V}_s^{ch} = \mathbf{V}_s^m$). We use the following steady-state mass conservation equations to keep track melting and melt extraction in matrix solid, matrix melt, and channel melt (Liang and Parmentier, 2010):

$$\nabla \cdot \left[(1-\psi)\rho_f \phi_m \mathbf{V}_f^m\right] = (1-\psi)\Gamma_m - (1-\psi)(\Gamma_m S + X), \quad (A.1)$$

$$\nabla \cdot \left[(1-\psi)\rho_s (1-\phi_m)\mathbf{V}_s^m\right] = -(1-\psi)\Gamma_m, \quad (A.2)$$

$$\nabla \cdot \left(\psi \rho_f \phi_{ch} \mathbf{V}_f^{ch}\right) = (1-\psi)(\Gamma_m S + X), \quad (A.3)$$

where ρ is the density; ϕ is the porosity; $\mathbf{V}$ is the velocity; S is the relative melt suction rate; ψ is the volume proportion of channel continuum; X accounts for the melt suction rate when there is no melting; subscript/superscript m, ch, s, f represent the matrix, channel, solid, and melt, respectively. (Key symbols are listed in Table A1.) The matrix melting rate (Γ_m) is calculated from pMELTS-derived melt productivity and solid upwelling rate using the expression:

$$\Gamma_m = \rho_s \frac{dF}{dz} \frac{(1-\phi_m)\mathbf{V}_s^m \cdot \mathbf{n_z}}{1-F}, \quad (A.4)$$

Table A1
Key symbols.

Variable	Meaning	Value
d_m, d_{ch}	Grain size of the matrix or channel	0.4–10 mm
F	Degree of melting experienced by the bulk solid	<0.25
k_ϕ^{iso}	Isotropic permeability	
k_ϕ^{add}	Additional anisotropic permeability on the easy-flow direction	
$\mathbf{k_f^{ch}}$	Permeability tensor for the channel	
L_{dc}	Width of decompaction channels	40–100 km
P_{pz}	Piezometric pressure	
S	Relative melt suction rate	
$\mathbf{V}_s^m, \mathbf{V}_f^m$	Velocity of the solid and melt in the matrix	
$\mathbf{V}_s^{ch}, \mathbf{V}_f^{ch}$	Velocity of the solid and melt in the channel	
β	Factor of permeability anisotropy for the shear-induced channels	0–15
ϕ_m, ϕ_{ch}	Porosity in the matrix or the channel	
Γ_m	Melting rate of the matrix	
η_f	Shear viscosity of the melt	10 Pa·s
η_s	Shear viscosity of the mantle	10^{19}–10^{21} Pa·s
ρ_f, ρ_s	Density of the melt and the solid	2700 and 3300 kg/m^3
$\Delta\rho$	Density difference of the melt and the solid	600 kg/m^3
θ	Local orientation of the channel	
Θ	Rotation tensor	
ψ	Volume proportion of channel	<0.10
ζ_s	Bulk viscosity of the mantle	Same as η_s

where $\mathbf{n_z}$ is the unit vertical vector, positive upward. Examples of calculated melting rate are shown in Fig. S3. Following previous applications of double-porosity models (Iwamori, 1993; Lundstrom, 2000; Jull et al., 2002; Liang and Parmentier, 2010), we assume that the melt suction rate is proportional to matrix melting rate. Given the matrix melting rate (Eq. (A.4)), the relative melt suction rate is independent of horizontal coordinate and takes on the general expression: We set the relative melt suction rate to be a constant so to satisfy the boundary condition of zero matrix porosity at LAB.

$$S = \frac{\int_0^{z_{LAB}} dz(1-\psi)\Gamma_m - \int_{z_{ch}}^{z_{LAB}} dz(1-\psi)X}{\int_{z_{ch}}^{z_{LAB}} dz(1-\psi)\Gamma_m}, \tag{A.5}$$

where $z_{LAB} = 100$ km is the height of LAB; z_{ch} is the height of replacive channels. If there is no melt suction rate when there is no melting ($X = 0$), the relative melt suction rate, for the case with shallow replacive channels would be 6, which is too high. Therefore, we set X for this case and use Eq. (A.5) to calculate the constant melting-independent melt suction rate. For the case with deep replacive channels, the relative melt suction rate is 1.16. The distribution of channels depends on the location of channels formed by different mechanisms. In this study, we examine three cases of channel distribution (Figs. 1b, 1c, and 1d).

The melt flow fields in the matrix and channel continua are governed by the generalized Darcy's law (McKenzie, 1984):

$$\phi_m\left(\mathbf{V}_f^m - \mathbf{V}_s^m\right) = -\frac{1}{\eta_f} k_\phi^m \cdot \nabla P_{pz}, \tag{A.6}$$

$$\phi_{ch}\left(\mathbf{V}_f^{ch} - \mathbf{V}_s^{ch}\right) = -\frac{1}{\eta_f} \mathbf{k}_\phi^{ch} \cdot \nabla P_{pz}, \tag{A.7}$$

$$\nabla P_{pz} = \eta_s \nabla^2 \mathbf{V}_s^m + \left(\zeta_s + \frac{1}{3}\eta_s\right)\nabla\left(\nabla \cdot \mathbf{V}_s^m\right) + \Delta\rho\mathbf{g}, \tag{A.8}$$

where $\mathbf{k}_\phi^{ch}$ is the permeability tensor for the channel continuum; P_{pz} is the piezometric pressure or the "pressure in excess of hydrostatic pressure" (Spiegelman and McKenzie, 1987); ζ_s and η_s are the bulk and shear viscosities of the solid; respectively; η_f is the shear viscosity of the melt; $\mathbf{g}$ is the gravitational acceleration vector; $\Delta\rho$ is the density difference between the solid and the melt. Eq. (A.8) states that the gradient of piezometric pressure arises from shear deformation in the solid, compaction in the solid, and buoyancy of the melt. A constant solid viscosity of 10^{19} Pa·s is used for most calculations. The effect of a higher viscosity is shown in Fig. S3.

The steady-state mass conservation equation for a trace element or radiogenic nuclide takes on the general expression (e.g. McKenzie, 1984; Jull et al., 2002; Liang and Parmentier, 2010):

$$\begin{aligned}
&\nabla \cdot \left((1-\psi)\rho_f\phi_m\mathbf{V}_f^m C_f^{m,i}\right) + \nabla \cdot \left(\rho_s(1-\psi)(1-\phi_m)\mathbf{V}_s^m C_s^{m,i}\right) \\
&\quad = -(1-\psi)\Gamma_m S C_f^{m,i} - (1-\psi)\rho_f\phi_m\left(\lambda_i C_f^{m,i} - \lambda_{i-1}C_f^{m,i-1}\right) \\
&\qquad - \rho_s(1-\psi)(1-\phi_m)\left(\lambda_i C_s^{m,i} - \lambda_{i-1}C_s^{m,i-1}\right),
\end{aligned} \tag{A.9}$$

$$C_s^{m,i} = k_i C_f^{m,i}, \tag{A.10}$$

where nuclide $i-1$ is the parent of i; λ is the decay constant which is set to zero for REE; k is the bulk partition coefficient. The trace elements in the present model include La, Ce, Nd, Sm, Eu, Gd, Dy, Y, and Yb. We also use Eqs. (A.9) and (A.10) to solve for concentrations of ^{234}U, ^{230}Th, and ^{226}Ra. The definition of the activity of radiogenic nuclide follows usual conventions (Elliott and Spiegelman, 2014). ^{238}U concentration will be calculated using (^{238}U/^{234}U) = 1 observed in all MORB samples (Elliott and Spiegelman, 2014). We use the starting mineral modes of Workman and Hart for DMM (2005), individual mineral/melt partition coefficient, and a linearized melting reaction to calculate the bulk partition coefficient of spinel lherzolite/harzburgite. For melting in the garnet stability field, we use pMELTS and DMM composition to derive garnet mode. Melting reaction and mineral-melt partition coefficients are from the literature (Baker and Stolper, 1994; Hauri et al., 1994; Wood et al., 1999; Salters et al., 2002; Kelemen et al., 2003; Sun and Liang, 2012; Yao et al., 2012; Wood and Blundy, 2014).

Next, we consider a matrix melt pocket that is extracted to the channel at location (x, y). Bulk partition coefficients for U, Th, and Ra in dunite are negligibly small. Therefore, reequilibration during transport in channels is governed by the time-dependent ordinary differential equations (Elliott and Spiegelman, 2014):

$$\frac{d^{234}\mathrm{U}}{dt} = 0, \tag{A.11}$$

$$\frac{d^{230}\mathrm{Th}}{dt} = -\lambda_{230\mathrm{Th}} \cdot {}^{230}\mathrm{Th} + \lambda_{234\mathrm{U}} \cdot {}^{234}\mathrm{U}, \tag{A.12}$$

$$\frac{d^{226}\mathrm{Ra}}{dt} = -\lambda_{226\mathrm{Ra}} \cdot {}^{226}\mathrm{Ra} + \lambda_{230\mathrm{Th}} \cdot {}^{230}\mathrm{Th}, \tag{A.13}$$

where the loss of ^{234}U is buffered by the decay of ^{238}U. Solutions of Eqs. (A.5)-(A.7) are given by Elliott and Spiegelman (2014) and can be integrated along streamlines of the channel melt (or in the melt focusing area) to obtain the concentration of ^{234}U, ^{230}Th, and ^{226}Ra in the channel melt at LAB (or the pooled channel melt). The concentration in the pooled melt is given by:

$$\overline{C_f^{ch,1}} \int_{\Omega_{ch}} dxdy \cdot (1-\psi)(\Gamma_m S + X) = \int_{\Omega_{ch}} dxdy \cdot C_f^{m,1} \cdot (1-\psi)(\Gamma_m S + X), \tag{A.14}$$

$$\overline{C_f^{ch,2}} \int_{\Omega_{ch}} dxdy \cdot (1-\psi)(\Gamma_m S + X) = \int_{\Omega_{ch}} dxdy \cdot \left[e^{-\lambda_2 \tau(x,y)} C_f^{m,2} + \frac{1-e^{-\lambda_2 \tau(x,y)}}{\lambda_2} \lambda_1 C_f^{m,1} \right] \cdot (1-\psi)(\Gamma_m S + X), \tag{A.15}$$

$$\overline{C_f^{ch,3}} \int_{\Omega_{ch}} dxdy \cdot (1-\psi)(\Gamma_m S + X) = \int_{\Omega_{ch}} dxdy \cdot \left[\begin{array}{l} e^{-\lambda_3 \tau(x,y)} C_f^{m,3} + \frac{e^{-\lambda_2 \tau(x,y)} - e^{-\lambda_3 \tau(x,y)}}{\lambda_3 - \lambda_2} \lambda_2 C_f^{m,2} \\ +\left(\frac{1-e^{-\lambda_3 \tau(x,y)}}{\lambda_3} - \frac{e^{-\lambda_2 \tau(x,y)} - e^{-\lambda_3 \tau(x,y)}}{\lambda_3 - \lambda_2}\right) \lambda_1 C_f^{m,1} \end{array} \right] \cdot (1-\psi)(\Gamma_m S + X), \tag{A.16}$$

where subscripts or superscripts 1, 2, and 3 are shorthand notation for ^{234}U, ^{230}Th, and ^{226}Ra; $\overline{C_f^{ch}}$ is the concentration of the pooled channel melt; Ω_{ch} is the melt pooling area of channels (e.g. Figs. S1 and S2); $\tau(x, y)$ is the melt transport time through the channel networks from a point (x, y) in the melting region to the decompaction channel at LAB. For simplicity, we neglect the transport time in the decompaction channel in this study as the melt flux is considerably higher there.

Finally, the concentration of the pooled melt, including contributions from both the channel and the matrix, can be calculated using the expression:

$$C^{Pooled} = \frac{\int_{DC} dL \cdot [(1-\psi)\phi_m V_f^m \cdot C_f^m] + \overline{C_f^{ch}} \cdot \int_{\Omega_{ch}} dxdy \cdot (1-\psi)(\Gamma_m S + X)}{\int_{DC} dL \cdot [(1-\psi)\phi_m V_f^m] + \int_{\Omega_{ch}} dxdy \cdot (1-\psi)(\Gamma_m S + X)}, \tag{A.17}$$

where DC is the domain boundary consisting of decompaction channels.

We use an iterative finite difference method to solve the porosities and velocities of the matrix and channel continua targeting a relative error of 1%. We then construct and solve the set of equations for the transport and fractionation of REE and radiogenic nuclides U, Th, and Ra. The numerical method is detailed in Liu (2018).

Appendix B. Supplementary material

Supplementary material related to this article can be found online at https://doi.org/10.1016/j.epsl.2019.115788.

References

Aharonov, E., Whitehead, J.A., Kelemen, P.B., Spiegelman, M., 1995. Channeling instability of upwelling melt in the mantle. J. Geophys. Res., Solid Earth 100 (B10), 20433–20450.

Baker, M.B., Stolper, E.M., 1994. Determining the composition of high-pressure mantle melts using diamond aggregates. Geochim. Cosmochim. Acta 58 (13), 2811–2827.

Behn, M.D., Grove, T.L., 2015. Melting systematics in mid-ocean ridge basalts: application of a plagioclase-spinel melting model to global variations in major element chemistry and crustal thickness. J. Geophys. Res., Solid Earth 120 (7), 4863–4886.

Bell, S., Ruan, Y., Forsyth, D.W., 2016. Ridge asymmetry and deep aqueous alteration at the trench observed from Rayleigh wave tomography of the Juan de Fuca plate. J. Geophys. Res., Solid Earth 121 (10), 7298–7321.

Bourdon, B., Goldstein, S.J., Bourlès, D., Murrell, M.T., Langmuir, C.H., 2000. Evidence from ^{10}Be and U series disequilibria on the possible contamination of mid-ocean ridge basalt glasses by sedimentary material. Geochem. Geophys. Geosyst. 1 (8).

Bourdon, B., Turner, S.P., Ribe, N.M., 2005. Partial melting and upwelling rates beneath the Azores from a U-series isotope perspective. Earth Planet. Sci. Lett. 239 (1–2), 42–56.

Bourdon, B., Zindler, A., Elliott, T., Langmuir, C.H., 1996. Constraints on mantle melting at mid-ocean ridges from global ^{238}U-^{230}Th disequilibrium data. Nature 384 (6606), 231–235.

Brunelli, D., Cipriani, A., Ottolini, L., Peyve, A., Bonatti, E., 2003. Mantle peridotites from the Bouvet Triple Junction Region, South Atlantic. Terra Nova 15 (3), 194–203.

Brunelli, D., Seyler, M., 2010. Asthenospheric percolation of alkaline melts beneath the St. Paul region (Central Atlantic Ocean). Earth Planet. Sci. Lett. 289 (3–4), 393–405.

Brunelli, D., Seyler, M., Cipriani, A., Ottolini, L., Bonatti, E., 2006. Discontinuous melt extraction and weak refertilization of mantle peridotites at the Vema Lithospheric Section (Mid-Atlantic Ridge). J. Petrol. 47 (4), 745–771.

Cooper, K.M., Goldstein, S.J., Sims, K.W., Murrell, M.T., 2003. Uranium-series chronology of Gorda Ridge volcanism: new evidence from the 1996 eruption. Earth Planet. Sci. Lett. 206 (3), 459–475.

D'Errico, M.E., Warren, J.M., Godard, M., 2016. Evidence for chemically heterogeneous Arctic mantle beneath the Gakkel Ridge. Geochim. Cosmochim. Acta 174, 291–312.

Dick, H.J.B., Natland, J.H., 1996. Late-stage melt evolution and transport in the shallow mantle beneath the East Pacific Rise. Proc. Ocean Drill. Program Sci. Results 147, 32.

Dreyer, B.M., Clague, D.A., Gill, J.B., 2013. Petrological variability of recent magmatism at Axial Seamount summit, Juan de Fuca Ridge. Geochem. Geophys. Geosyst. 14 (10), 4306–4333.

Elkins, L.J., Bourdon, B., Lambart, S., 2019. Testing pyroxenite versus peridotite sources for marine basalts using U-series isotopes. Lithos 332–333, 226–244.

Elkins, L.J., Hamelin, C., Blichert-Toft, J., Scott, S.R., Sims, K.W.W., Yeo, I.A., Devey, C.W., Pedersen, R.B., 2016a. North Atlantic hotspot-ridge interaction near Jan Mayen Island. Geochem. Perspect. Lett. 2, 55–67.

Elkins, L.J., Scott, S.R., Sims, K.W.W., Rivers, E.R., Devey, C.W., Reagan, M.K., Hamelin, C., Pedersen, R.B., 2016b. Exploring the role of mantle eclogite at mid-ocean ridges and hotspots: U-series constraints on Jan Mayen Island and the Kolbeinsey Ridge. Chem. Geol. 444, 128–140.

Elkins, L.J., Sims, K.W.W., Prytulak, J., Blichert-Toft, J., Elliott, T., Blusztajn, J., Fretzdorff, S., Reagan, M., Haase, K., Humphris, S., Schilling, J.G., 2014. Melt generation beneath Arctic Ridges: implications from U decay series disequilibria in the Mohns, Knipovich, and Gakkel Ridges. Geochim. Cosmochim. Acta 127, 140–170.

Elkins, L.J., Sims, K.W.W., Prytulak, J., Elliott, T., Mattielli, N., Blichert-Toft, J., Blusztajn, J., Dunbar, N., Devey, C., Mertz, D.F., Schilling, J.G., Murrell, M., 2011. Understanding melt generation beneath the slow-spreading Kolbeinsey Ridge using ^{238}U, ^{230}Th, and ^{231}Pa excesses. Geochim. Cosmochim. Acta 75 (21), 6300–6329.

Elliott, T., Spiegelman, M., 2014. Melt migration in oceanic crustal production: a U-series perspective. In: Treatise on Geochemistry, vol. 3, pp. 465–510.

Forsyth, D.W., 1993. Crustal thickness and the average depth and degree of melting in fractional melting models of passive flow beneath mid-ocean ridges. J. Geophys. Res., Solid Earth 98 (B9), 16073–16079.

Forsyth, D.W., Scheirer, D.S., Webb, S.C., Dorman, L.M., Orcutt, J.A., Harding, A.J., Detrick, R.S., Shen, Y., Wolfe, C.J., Canales, J.P., Toomey, D.R., Sheehan, A.F., Solomon, S.C., Wilcock, W.S.D., 1998. Imaging the deep seismic structure beneath a mid-ocean ridge: the MELT experiment. Science 280 (5367), 1215–1220.

Ghiorso, M.S., Hirschmann, M.M., Reiners, P.W., Kress, V.C., 2002. The pMELTS: a revision of MELTS for improved calculation of phase relations and major element partitioning related to partial melting of the mantle to 3 GPa. Geochem. Geophys. Geosyst. 3 (5), 1–35.

Goldstein, S.J., Murrell, M.T., Janecky, D.R., 1989. Th and U isotopic systematics of basalts from the Juan de Fuca and Gorda Ridges by mass spectrometry. Earth Planet. Sci. Lett. 96 (1), 134–146.

Goldstein, S.J., Murrell, M.T., Janecky, D.R., Delaney, J.R., Clague, D.A., 1992. Geochronology and petrogenesis of MORB from the Juan de Fuca and Gorda ridges by ^{238}U-^{230}Th disequilibrium. Earth Planet. Sci. Lett. 109 (1), 255–272.

Goldstein, S.J., Murrell, M.T., Williams, R.W., 1993. ^{231}Pa and ^{230}Th chronology of mid-ocean ridge basalts. Earth Planet. Sci. Lett. 115 (1), 151–159.

Hauri, E.H., Wagner, T.P., Grove, T.L., 1994. Experimental and natural partitioning of Th, U, Pb and other trace elements between garnet, clinopyroxene and basaltic melts. Chem. Geol. 117 (1), 149–166.

Hebert, L.B., Montési, L.G.J., 2010. Generation of permeability barriers during melt extraction at mid-ocean ridges. Geochem. Geophys. Geosyst. 11 (12).

Hellebrand, E., Snow, J., Mostefaoui, S., Hoppe, P., 2005. Trace element distribution between orthopyroxene and clinopyroxene in peridotites from the Gakkel Ridge: a SIMS and NanoSIMS study. Contrib. Mineral. Petrol. 150 (5), 486–504.

Hellebrand, E., Snow, J.E., Hoppe, P., Hofmann, A.W., 2002. Garnet-field melting and late-stage refertilization in 'Residual' abyssal peridotites from the Central Indian Ridge. J. Petrol. 43 (12), 2305–2338.

Hesse, M.A., Schiemenz, A.R., Liang, Y., Parmentier, E.M., 2011. Compaction–dissolution waves in an upwelling mantle column. Geophys. J. Int. 187 (3), 1057–1075.

Iwamori, H., 1993. Dynamic disequilibrium melting model with porous flow and diffusion-controlled chemical equilibration. Earth Planet. Sci. Lett. 114 (2), 301–313.

Johnson, K.T.M., Dick, H.J.B., 1992. Open system melting and temporal and spatial variation of peridotite and basalt at the Atlantis II Fracture Zone. J. Geophys. Res., Solid Earth 97 (B6), 9219–9241.

Johnson, K.T.M., Dick, H.J.B., Shimizu, N., 1990. Melting in the oceanic upper mantle: an ion microprobe study of diopsides in abyssal peridotites. J. Geophys. Res., Solid Earth 95 (B3), 2661–2678.

Jull, M., Kelemen, P.B., Sims, K., 2002. Consequences of diffuse and channelled porous melt migration on uranium series disequilibria. Geochim. Cosmochim. Acta 66 (23), 4133–4148.

Kelemen, P.B., Braun, M., Hirth, G., 2000. Spatial distribution of melt conduits in the mantle beneath oceanic spreading ridges: observations from the Ingalls and Oman ophiolites. Geochem. Geophys. Geosyst. 1 (7).

Kelemen, P.B., Hirth, G., Shimizu, N., Spiegelman, M., Dick, H.J.B., 1997. A review of melt migration processes in the adiabatically upwelling mantle beneath Oceanic Spreading Ridges. Philos. Trans. R. Soc., Math. Phys. Eng. Sci. 355 (1723), 283–318.

Kelemen, P.B., Yogodzinski, G.M., Scholl, D.W., 2003. Along-strike variation in the Aleutian Island Arc: genesis of high Mg# andesite and implications for Continental Crust. In: Inside the Subduction Factory, pp. 223–276.

Keller, T., Katz, R.F., Hirschmann, M.M., 2017. Volatiles beneath mid-ocean ridges: deep melting, channelised transport, focusing, and metasomatism. Earth Planet. Sci. Lett. 464, 55–68.

Key, K., Constable, S., Liu, L., Pommier, A., 2013. Electrical image of passive mantle upwelling beneath the northern East Pacific Rise. Nature 495 (7442), 499–502.

Kohlstedt, D.L., Holtzman, B.K., 2009. Shearing melt out of the Earth: an experimentalist's perspective on the influence of deformation on melt extraction. Annu. Rev. Earth Planet. Sci. 37 (1), 561–593.

Landwehr, D., Blundy, J., Chamorro-Perez, E.M., Hill, E., Wood, B., 2001. U-series disequilibria generated by partial melting of spinel lherzolite. Earth Planet. Sci. Lett. 188 (3–4), 329–348.

Lassiter, J.C., Byerly, B.L., Snow, J.E., Hellebrand, E., 2014. Constraints from Os-isotope variations on the origin of Lena Trough abyssal peridotites and implications for the composition and evolution of the depleted upper mantle. Earth Planet. Sci. Lett. 403, 178–187.

Liang, Y., Liu, B., 2016. Simple models for disequilibrium fractional melting and batch melting with application to REE fractionation in abyssal peridotites. Geochim. Cosmochim. Acta 173, 181–197.

Liang, Y., Parmentier, E.M., 2010. A two-porosity double lithology model for partial melting, melt transport and melt–rock reaction in the mantle: mass conservation equations and trace element transport. J. Petrol. 51 (1–2), 125–152.

Liang, Y., Peng, Q., 2010. Non-modal melting in an upwelling mantle column: steady-state models with applications to REE depletion in abyssal peridotites and the dynamics of melt migration in the mantle. Geochim. Cosmochim. Acta 74 (1), 321–339.

Liang, Y., Schiemenz, A., Hesse, M.A., Parmentier, E.M., Hesthaven, J.S., 2010. High-porosity channels for melt migration in the mantle: top is the dunite and bottom is the harzburgite and lherzolite. Geophys. Res. Lett. 37 (15).

Liang, Y., Schiemenz, A., Hesse, M.A., Parmentier, E.M., 2011. Waves, channels, and the preservation of chemical heterogeneities during melt migration in the mantle. Geophys. Res. Lett. 38 (20).

Liu, B., 2018. Melt Migration Dynamics and Trace Element Fractionation Beneath Mid-Ocean Ridges. Brown University Thesis.

Liu, B., Liang, Y., 2017. An introduction of Markov chain Monte Carlo method to geochemical inverse problems: reading melting parameters from REE abundances in abyssal peridotites. Geochim. Cosmochim. Acta 203, 216–234.

Lundstrom, C.C., Gill, J., Williams, Q., Perfit, M.R., 1995. Mantle melting and basalt extraction by equilibrium porous flow. Science 270 (5244), 1958–1961.

Lundstrom, C.C., Gill, J., Williams, Q., Hanan, B., 1998. Investigating solid mantle upwelling beneath mid-ocean ridges using U-series disequilibria. II. A local study at 33 S Mid-Atlantic Ridge. Earth Planet. Sci. Lett. 157 (3–4), 167–181.

Lundstrom, C.C., Sampson, D., Perfit, M., Gill, J., Williams, Q., 1999. Insights into mid-ocean ridge basalt petrogenesis: U-series disequilibria from the Siqueiros Transform, Lamont Seamounts, and East Pacific Rise. J. Geophys. Res., Solid Earth 104 (B6), 13035–13048.

Lundstrom, C.C., 2000. Models of U-series disequilibria generation in MORB: the effects of two scales of melt porosity. Phys. Earth Planet. Inter. 121 (3–4), 189–204.

Mallick, S., Dick, H.J.B., Sachi-Kocher, A., Salters, V.J.M., 2014. Isotope and trace element insights into heterogeneity of subridge mantle. Geochem. Geophys. Geosyst. 15 (6), 2438–2453.

McKenzie, D., 1984. The generation and compaction of partially molten rock. J. Petrol. 25 (3), 713–765.

McKenzie, D., 1985. ^{230}Th-^{238}U disequilibrium and the melting processes beneath ridge axes. Earth Planet. Sci. Lett. 72 (2–3), 149–157.

Miller, K.J., Zhu, W.-L., Montési, L.G.J., Gaetani, G.A., 2014. Experimental quantification of permeability of partially molten mantle rock. Earth Planet. Sci. Lett. 388, 273–282.

Morgan, Z., Liang, Y., 2005. An experimental study of the kinetics of lherzolite reactive dissolution with applications to melt channel formation. Contrib. Mineral. Petrol. 150 (4), 369–385.

Nye, J.F., 1985. Physical Properties of Crystals: Their Representation by Tensors and Matrices. Oxford University Press.

O'Hara, M.J., 1985. Importance of the 'shape' of the melting regime during partial melting of the mantle. Nature 314 (6006), 58–62.

Peate, D.W., Hawkesworth, C.J., van Calsteren, P.W., Taylor, R.N., Murton, B.J., 2001. ^{238}U–^{230}Th constraints on mantle upwelling and plume–ridge interaction along the Reykjanes Ridge. Earth Planet. Sci. Lett. 187 (3), 259–272.

Pertermann, M., Hirschmann, M.M., Hametner, K., Günther, D., Schmidt, M.W., 2004. Experimental determination of trace element partitioning between garnet and silica-rich liquid during anhydrous partial melting of MORB-like eclogite. Geochem. Geophys. Geosyst. 5 (5).

Phillips, O.M., 1991. Flow and Reactions in Permeable Rocks. Cambridge University Press.

Phipps Morgan, J., 1987. Melt migration beneath mid-ocean spreading centers. Geophys. Res. Lett. 14 (12), 1238–1241.

Phipps Morgan, J., Holtzman, B.K., 2005. Vug waves: a mechanism for coupled rock deformation and fluid migration. Geochem. Geophys. Geosyst. 6 (8).

Qin, Z., 1992. Disequilibrium partial melting model and its implications for trace element fractionations during mantle melting. Earth Planet. Sci. Lett. 112 (1), 75–90.

Richardson, C., McKenzie, D., 1994. Radioactive disequilibria from 2D models of melt generation by plumes and ridges. Earth Planet. Sci. Lett. 128 (3), 425–437.

Ross, K., Elthon, D., 1997. Extreme incompatible trace-element depletion of diopside in residual mantle from south of the Kane fracture zone. Proc. Ocean Drill. Program Sci. Results 153, 13.

Rubin, K.H., Macdougall, J.D., 1988. ^{226}Ra excesses in mid-ocean-ridge basalts and mantle melting. Nature 335 (6186), 158–161.

Rubin, K.H., van der Zander, I., Smith, M.C., Bergmanis, E.C., 2005. Minimum speed limit for ocean ridge magmatism from ^{210}Pb-^{226}Ra-^{230}Th disequilibria. Nature 437 (7058), 534–538.

Russo, C.J., Rubin, K.H., Graham, D.W., 2009. Mantle melting and magma supply to the Southeast Indian Ridge: the roles of lithology and melting conditions from U-series disequilibria. Earth Planet. Sci. Lett. 278 (1–2), 55–66.

Saal, A.E., Van Orman, J.A., 2004. The ^{226}Ra enrichment in oceanic basalts: evidence for melt-cumulate diffusive interaction processes within the oceanic lithosphere. Geochem. Geophys. Geosyst. 5 (2).

Salters, V.J.M., Dick, H.J.B., 2002. Mineralogy of the mid-ocean-ridge basalt source from neodymium isotopic composition of abyssal peridotites. Nature 418 (6893), 68–72.

Salters, V.J.M., Longhi, J.E., Bizimis, M., 2002. Near mantle solidus trace element partitioning at pressures up to 3.4 GPa. Geochem. Geophys. Geosyst. 3 (7), 1–23.

Salters, V.J.M., Stracke, A., 2004. Composition of the depleted mantle. Geochem. Geophys. Geosyst. 5 (5), Q05B07.

Sanfilippo, A., Salters, V., Tribuzio, R., Zanetti, A., 2019. Role of ancient, ultra-depleted mantle in Mid-Ocean-Ridge magmatism. Earth Planet. Sci. Lett. 511, 89–98.

Schiemenz, A., Liang, Y., Parmentier, E.M., 2011. A high-order numerical study of reactive dissolution in an upwelling heterogeneous mantle-I. Channelization, channel lithology and channel geometry. Geophys. J. Int. 186 (2), 641–664.

Scott, S.R., Ramos, F.C., Gill, J.B., 2018. Spreading dynamics of an intermediate ridge: insights from U-series disequilibria, Endeavour Segment, Juan de Fuca Ridge. J. Petrol. 59 (10), 1847–1868.

Seyler, M., Bonatti, E., 1997. Regional-scale melt-rock interaction in lherzolitic mantle in the Romanche Fracture Zone (Atlantic Ocean). Earth Planet. Sci. Lett. 146 (1–2), 273–287.

Seyler, M., Brunelli, D., Toplis, M.J., Mével, C., 2011. Multiscale chemical heterogeneities beneath the eastern Southwest Indian Ridge (52°E–68°E): trace element compositions of along-axis dredged peridotites. Geochem. Geophys. Geosyst. 12 (9).

Sims, K.W., DePaolo, D.J., Murrell, M.T., Baldridge, W.S., Goldstein, S.J., Clague, D.A., 1995. Mechanisms of magma generation beneath Hawaii and mid-ocean ridges: uranium/thorium and samarium/neodymium isotopic evidence. Science 267 (5197), 508–512.

Sims, K.W.W., Goldstein, S.J., Blichert-toft, J., Perfit, M.R., Kelemen, P., Fornari, D.J., Michael, P., Murrell, M.T., Hart, S.R., DePaolo, D.J., Layne, G., Ball, L., Jull, M., Bender, J., 2002. Chemical and isotopic constraints on the generation and transport of magma beneath the East Pacific Rise. Geochim. Cosmochim. Acta 66 (19), 3481–3504.

Snow, J.E., 1993. The Isotope Geochemistry of Abyssal Peridotites and Related Rocks (No. WHOI-93-36).

Sparks, D.W., Parmentier, E.M., 1991. Melt extraction from the mantle beneath spreading centers. Earth Planet. Sci. Lett. 105 (4), 368–377.

Spiegelman, M., 1993. Physics of melt extraction: theory, implications and applications. Philos. Trans. R. Soc., Math. Phys. Eng. Sci. 342 (1663), 23–41.

Spiegelman, M., 1996. Geochemical consequences of melt transport in 2-D: the sensitivity of trace elements to mantle dynamics. Earth Planet. Sci. Lett. 139 (1), 115–132.

Spiegelman, M., Elliott, T., 1993. Consequences of melt transport for uranium series disequilibrium in young lavas. Earth Planet. Sci. Lett. 118 (1–4), 1–20.

Spiegelman, M., Kelemen, P.B., Aharonov, E., 2001. Causes and consequences of flow organization during melt transport: the reaction infiltration instability in compatible media. J. Geophys. Res., Solid Earth 106 (B2), 2061–2077.

Spiegelman, M., McKenzie, D., 1987. Simple 2-D models for melt extraction at mid-ocean ridges and island arcs. Earth Planet. Sci. Lett. 83 (1), 137–152.

Sturm, M.E., Goldstein, S.J., Klein, E.M., Karson, J.A., Murrell, M.T., 2000. Uranium-series age constraints on lavas from the axial valley of the Mid-Atlantic Ridge, MARK area. Earth Planet. Sci. Lett. 181 (1), 61–70.

Sun, C., Liang, Y., 2012. Distribution of REE between clinopyroxene and basaltic melt along a mantle adiabat: effects of major element composition, water, and temperature. Contrib. Mineral. Petrol. 163 (5), 807–823.

Turner, A.J., Katz, R.F., Behn, M.D., 2015a. Grain-size dynamics beneath mid-ocean ridges: implications for permeability and melt extraction. Geochem. Geophys. Geosyst. 16 (3), 925–946.

Turner, S., Kokfelt, T., Hauff, F., Haase, K., Lundstrom, C., Hoernle, K., Yeo, I., Devey, C., 2015b. Mid-ocean ridge basalt generation along the slow-spreading, South Mid-Atlantic Ridge (5–11°S): inferences from ^{238}U–^{230}Th–^{226}Ra disequilibria. Geochim. Cosmochim. Acta 169, 152–166.

Van Orman, J.A., Grove, T.L., Shimizu, N., 1998. Uranium and thorium diffusion in diopside. Earth Planet. Sci. Lett. 160 (3–4), 505–519.

Van Orman, J.A., Grove, T.L., Shimizu, N., 2001. Rare earth element diffusion in diopside: influence of temperature, pressure, and ionic radius, and an elastic model for diffusion in silicates. Contrib. Mineral. Petrol. 141 (6), 687–703.

Wark, D.A., Watson, E.B., 1998. Grain-scale permeabilities of texturally equilibrated, monomineralic rocks. Earth Planet. Sci. Lett. 164 (3–4), 591–605.

Warren, J.M., 2016. Global variations in abyssal peridotite compositions. Lithos 248–251, 193–219.

Warren, J.M., 2007. Geochemical and Rheological Constraints on the Dynamics of the Oceanic Upper Mantle. Massachusetts Institute of Technology.

Warren, J.M., Shimizu, N., 2010. Cryptic variations in abyssal peridotite compositions: evidence for shallow-level melt infiltration in the oceanic lithosphere. J. Petrol. 51 (1–2), 395–423.

Waters, C.L., Sims, K.W.W., Klein, E.M., White, S.M., Reagan, M.K., Girard, G., 2013. Sill to surface: linking young off-axis volcanism with subsurface melt at the overlapping spreading center at 9°03′N East Pacific Rise. Earth Planet. Sci. Lett. 369–370, 59–70.

White, R.S., McKenzie, D., O'Nions, R.K., 1992. Oceanic crustal thickness from seismic measurements and rare earth element inversions. J. Geophys. Res., Solid Earth 97 (B13), 19683–19715.

White, W.M., Klein, E.M., 2014. 4.13 – Composition of the oceanic crust. In: Turekian, K.K. (Ed.), Treatise on Geochemistry, second edition. Elsevier, Oxford, pp. 457–496.

Wood, B.J., Blundy, J.D., 2014. 3.11 – Trace element partitioning: the influences of ionic radius, cation charge, pressure, and temperature. In: Turekian, K.K. (Ed.), Treatise on Geochemistry, second edition. Elsevier, Oxford, pp. 421–448.

Wood, B.J., Blundy, J.D., Robinson, J.A.C., 1999. The role of clinopyroxene in generating U-series disequilibrium during mantle melting. Geochim. Cosmochim. Acta 63 (10), 1613–1620.

Workman, R.K., Hart, S.R., 2005. Major and trace element composition of the depleted MORB mantle (DMM). Earth Planet. Sci. Lett. 231 (1–2), 53–72.

Yang, Y., Forsyth, D.W., Weeraratne, D.S., 2007. Seismic attenuation near the East Pacific Rise and the origin of the low-velocity zone. Earth Planet. Sci. Lett. 258 (1), 260–268.

Yao, L., Sun, C., Liang, Y., 2012. A parameterized model for REE distribution between low-Ca pyroxene and basaltic melts with applications to REE partitioning in low-Ca pyroxene along a mantle adiabat and during pyroxenite-derived melt and peridotite interaction. Contrib. Mineral. Petrol. 164 (2), 261–280.

Zhu, W.-L., Hirth, G., 2003. A network model for permeability in partially molten rocks. Earth Planet. Sci. Lett. 212 (3–4), 407–416.